

ADA 079858

6

A NUMERICAL STUDY OF NORMAL-SHOCK/
TURBULENT BOUNDARY LAYER INTERACTIONS

DDC
RECEIVED
JAN 28 1980
A

DDC FILE COPY

9

14 Master's THESIS

AFIT/GAE/AA/79D-8

10

Lowell C. Keel
Major USAF

16 2307

17 N4

11 hlec 79

12 77

Approved for public release; distribution unlimited

AFIT/GAE/AA/79D-8

A NUMERICAL STUDY OF NORMAL-SHOCK/
TURBULENT BOUNDARY LAYER INTERACTIONS

THESIS

Presented to the Faculty of the School of Engineering[✓]
of the Air Force Institute of Technology
Air University
in Partial Fulfillment of the
Requirements for the Degree of
Master of Science

by

Lowell C. Keel

Major USAF

Graduate Aeronautical Engineering

December 1979

Accession For	
NPIS GRA&I	<input checked="" type="checkbox"/>
DCS TAB	<input type="checkbox"/>
Unannounced	<input type="checkbox"/>
Publication	<input type="checkbox"/>

10
11
12
13
14
15
16
17
18
19
20
21
22
23
24
25
26
27
28
29
30
31
32
33
34
35
36
37
38
39
40
41
42
43
44
45
46
47
48
49
50
51
52
53
54
55
56
57
58
59
60
61
62
63
64
65
66
67
68
69
70
71
72
73
74
75
76
77
78
79
80
81
82
83
84
85
86
87
88
89
90
91
92
93
94
95
96
97
98
99
100

A

Approved for public release; distribution unlimited.

Preface

The study reported herein is the culmination of a desire which I have had for over twelve years. My inability to predict separation and reattachment of turbulent boundary layers in the influence of strong adverse pressure gradients in several previous efforts has made this study very self satisfying. When faced with the task of finding a thesis topic, I decided on two personal objectives. First, I wanted to improve my understanding of current numerical techniques and the state of their application to aerodynamics. Second, I wanted to study the transonic interaction of a shock wave with a turbulent boundary layer. I was both surprised and pleased to find that Capt John Shea had accomplished and reported in the last year almost exactly what I wanted to undertake. The effort reported herein has satisfied both of my personal objectives by extending Shea's numerical study of normal-shock/turbulent boundary layer interactions.

I would like to thank Capt Shea for his initial work, instruction, and guidance in the early phases of this thesis effort. I also appreciate the help given to me by Maj Steve Koob, Capt Jim Marsh, Dr. Charles Jobe, Dr. Will Hankey and Lt. John Waskiewicz.

I would also like to publicly thank Lt Robert Roach, who has served as my principal advisor since Capt Shea left AFIT in July, for his guidance and continued interest. For his sponsorship, friendship, and continued advice and encouragement, I am truly indebted to Dr. Joe Shang. I give my very special thanks to my wife Mary for her patience and understanding. Finally, I express my appreciation to Carla Dakhteh for her typing assistance.

Contents

	<u>Page</u>
Preface	ii
List of Figures	v
List of Tables	vii
Abstract	viii
Nomenclature	ix
I. Introduction	1
Background	1
Investigation Objectives	8
II. Approach	9
Base Line Case	9
Wall Boundary	12
Inflow Boundary	14
Supersonic Center Line Boundary	14
Subsonic Center Line Boundary	14
Outflow Boundary	15
Other Studies	16
Outflow Boundary Position	16
Mach Number Variation	17
III. Discussion and Results	18
Introduction	18
Identification of Results	18
Solution Convergence	18
Base Line Results	22
Boundary Conditions	23
Outflow Boundary Conditions	29
Center Line Boundary Conditions	32
Outflow Boundary Location	35
Mach Number Variation	36
Three-Dimensional Effects	39
Conclusions	48

Contents

	<u>Page</u>
IV. Recommendations and Suggestions	49
Bibliography	50
Appendix A: A Description of the Finite Difference Method Used . .	54
Appendix B: Boundary Condition Supporting Equations	61

List of Figures

<u>Figure</u>		<u>Page</u>
1	Sources of Normal-Shock Turbulent Boundary Layer Interactions in Nature	2
2	Seddon's Normal-Shock Turbulent Boundary Layer Interaction Model	6
3	Normal-Shock/Turbulent Boundary Layer Interaction Experimental Configurations	11
4	Boundary Condition Region Definitions	13
5	Base Line Case (O-Series) Convergence Plot	21
6	Experimental and Numerical Mach Contours for Base Line Case	23
7	Base Line Case Experimental and Numerical Longitudinal Total Velocity Profiles	26
8	Base Line Case Experimental and Numerical Transverse Total Velocity Profiles	27
9	Mach Contours Depicting Ill-treatment of Outflow Boundary Conditions	30
10	Transverse Total Velocity Profiles for Various Center Line Boundary Treatment (Data, O, K, L, M, N)	33
11	Mach Contours Depicting Shock Implementation Difficulty	34
12	Transverse Total Velocity Profiles for Various Outflow Boundary Treatment (Data, O, P, S, J)	37
13	Mach 1.30 and 1.40 Total Velocity Profiles (Experimental and Computed)	38
14	Transverse Total Velocity Profiles for Various Attempted Corrections (Data, O, B, T, I, U)	40
15	Mach Contour Distortion for Attempted 3-D Correction (I-Series)	42
16	Mach Contours Depicting Improved Shock-Center Line Structure With Corrected Outflow Mass Rate (O & T - Series)	43

<u>Figure</u>		<u>Page</u>
17	Convergence Plots for T and U Series Computations . .	45
18	Mach Contours Depicting Shock Movement with Attempted 3-D and Mass Flow Rate Corrections (U-Series)	46
19	Transverse Total Velocity Profiles of Sequential Numerical Results Compared to Experiment (U-Series).	47
20	Computational Mesh Structure	56

List of Tables

<u>Table</u>		<u>Page</u>
I	Computation Code Identification Key	19
II	Difference Equation Type Definition	20

Abstract

The hybrid finite difference code developed by MacCormack was applied to the investigation of transonic normal-shock turbulent boundary layer interactions. The computations were performed for the half plane of a symmetric two dimensional duct by establishing a symmetry boundary condition at the upper boundary. Both first and second order center line boundary conditions were imposed with no measurable difference observed. A two-point linear extrapolation of the primitive variable was unsuccessfully attempted at the subsonic outflow boundary, but a simple zero gradient condition gave satisfactory results at four different outflow boundary positions relative to the shock wave. Numerical results ($M_{\infty} = 1.51, 1.40$ and 1.30 $Re = 3 \times 10^6$ per ft) were compared with the experimental data reported by Abbiss and East. Even though the data exhibit three-dimensional effects, the two-dimensional computations show agreement within approximately 10%. The differences observed in the numerical-experimental comparisons were all consistent with expected three-dimensional trends. Although not conclusive, the potential of adding simple three-dimensional corrections to the two-dimensional code shows promise for improving the experimental-numerical agreement.

Nomenclature

English Symbols

a	Spec of sound
c_f	Local coefficient of friction
c_p	Specific heat at constant pressure, for air 6006 ft ² /sec R
c_v	Specific heat at constant volume, for air 4290 ft ² /sec R
e_t	Total energy per unit volume
e_i	Specific internal energy $e_t = 0.5 (u^2 + v^2) + e_i/\rho$
H, h	Enthalpies, $H = h + \frac{u^2 + v^2}{2}$
k	Coefficient of heat conductivity
M	Mach number
p	Pressure
R	Gas constant, 1716 ft ² /sec R for air $R = c_p - c_v$
Re	Reynolds number
RL	Reference length
T	Temperature
t_{ch}	Characteristic time, $(X_{I=1} - X_{I=IL})/U_\infty$
u	Velocity component in X direction
v	Velocity component in Y direction
x, y	Reference coordinate system with x parallel to wall (direction of mean flow) and y perpendicular to the wall

Greek Symbols

α	Local flow direction measured counterclockwise from the x axis
Δ	Finite difference differential element
γ	Ratio of specific heats, c_p/c_v

δ	Boundary layer thickness
δ^*	Boundary layer displacement thickness
γ	Viscosity coefficient, $\lambda = -2/3 \mu$
μ	Molecular viscosity
ν	Kinematic viscosity, μ/ρ
ρ	Density
τ	Shear stress

Subscripts and Superscripts

∞	Free stream or unperturbed condition
i	Index for computational mesh in x direction, $i = 1$ at inflow boundary
j	Index for computational mesh in y direction, $j = 1.5$ at wall
n, m	Time indices
o	Total or stagnation condition
$()_{x,y}$	Derivative with respect to x, y

Computer Code Variables

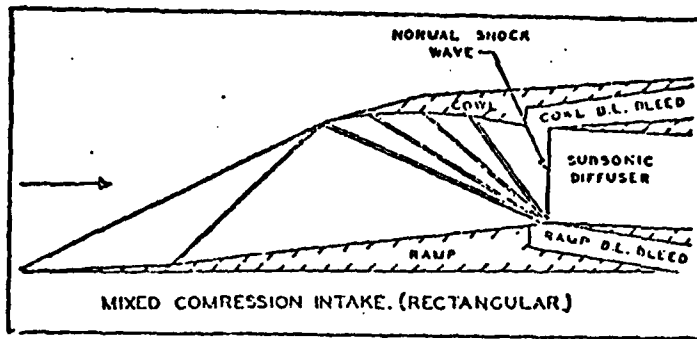
I	Column index for parameter storage (I fixed for any x location)
IL	Outflow boundary value of I index
$ILM1$	$IL-1$
$ILM2$	$IL-2$
J	Row index for parameter storage (J fixed for any y location)
JL	Center line boundary value of J index
$JLM1$	$JL-1$
$JLM2$	$JL-2$

† Introduction

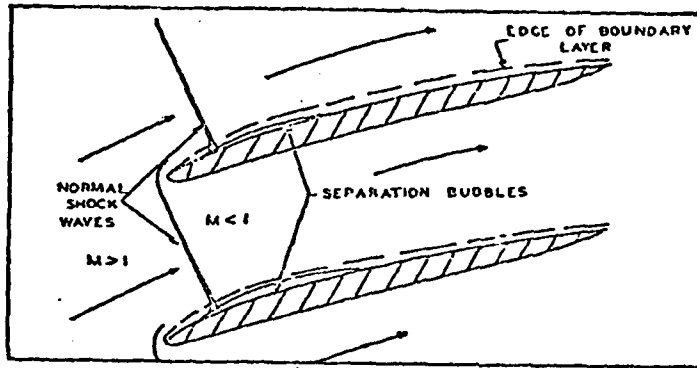
Background

Green (Ref 9) and Schofield (Ref 23) have pointed out that shock-boundary layer interactions are the predominant phenomena in many aerodynamic problems of interest. More specifically, normal-shock turbulent boundary layer interactions are found; (1) in transonic and supersonic inlets, (2) on transonic wings, (3) in compressor cascades, (4) on rotor tips, (5) in nozzles, and (6) on flow over control surfaces and high lift systems (see Figure 1). Although they have been a primary subject of study for over thirty years, very little progress had been realized in the prediction of strong interactions until the last three to five years. The lack of progress was due to the complex nature of the flow which is produced, and the nonlinearity of the differential equations required to model the flow. The application of today's high speed digital computers and modern numerical techniques (Refs 2, 5, 6, 14, 16, 20, 21 25-31) shows great promise of providing useful engineering solutions to many interaction problems.

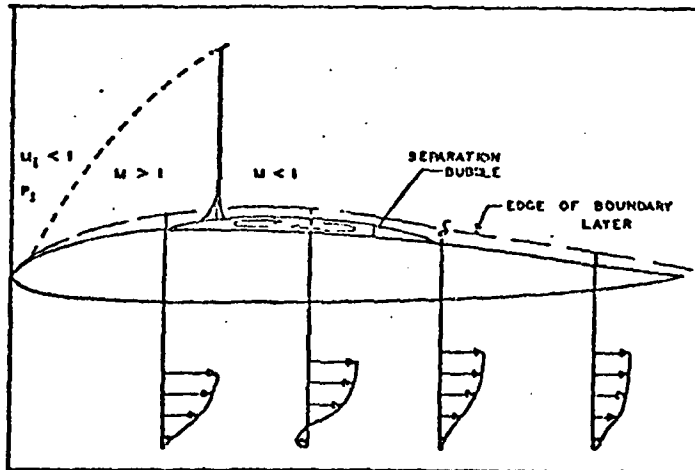
First a brief discussion of the physical phenomenon is provided. The viscous flow over any solid surface results in a boundary layer near the surface. If there were no boundary layer, a shock could theoretically be generated at or reflected from the solid surface. However, in the presence of a boundary layer, which is always physically present, an abrupt pressure rise, such as that caused by an impinging shock wave, cannot occur at the solid surface. The subsonic part of the boundary layer is unable to support such a sharp pressure change. Consequently, the pressure rise is spread upstream in the subsonic region of the boundary layer. This pressure rise causes a sudden increase in the boundary layer



a. TYPICAL SUPERSONIC AIR INTAKE



b. TRANSONIC COMPRESSOR BLADING NEAR TIPS



c. TRANSONIC AIRFOIL INTERACTION

Figure 1. Sources of Normal-Shock/Turbulent Boundary Layer Interactions in Nature

displacement thickness and precipitates compression waves in the supersonic region of the boundary layer. The pressure rise is therefore spread smoothly over a distance on the wall even though it is more sharply defined across the shock wave in the outer flow. The distance over which the pressure rise is spread is on the order of the undisturbed boundary layer thickness unless separation is induced. For cases where the boundary layer separates the affected region can be much larger (Ref 5:4-5). This shock wave configuration is commonly called a lambda shock, and the point where the shock and the compression waves meet is known as the bifurcation point.

Shock boundary layer interactions are usually divided into two major classes commonly denoted as strong and weak interactions. The classification is dependent on whether or not boundary layer separation effects on the global flow result from the interaction. Thus, a weak shock interaction may produce a limited separation bubble provided it does not noticeably alter the global flow field. Shock-boundary layer interactions are often further subclassified by the character of the shock and the surface configuration such as: (1) incident oblique shock wave, (2) compression corner, (3) forward facing step, (4) rearward facing step, and (5) normal shock wave. Interactions of shock waves with laminar boundary layers are often studied even though they are rarely found in practical applications.

The common occurrence of shock-boundary layer interactions and the predominant nature of their effect on flow phenomena justify continued effort in the development of accurate prediction techniques for such flows. Green (Ref 9) provided an excellent historical background (prior to 1969) and technical review of this subject in a von Karman Institute short course on the subject of shock-boundary layer interactions.

Schofield (Ref 23) also reviewed the subject and recommended an extensive experimental program to advance existing understanding of such interactions. Analytical, experimental and numerical approaches have been applied to the problem of developing prediction techniques for shock-boundary layer interactions.

The analytical approach inherently requires that the governing equations be extensively simplified before a solution can be obtained. Analytical solutions have been developed for inviscid flows, one-dimensional viscous flows, and flows very close to Mach 1.0. However, the mixture of subsonic, supersonic, viscous, and separation regions which all required simultaneous treatment strong normal-shock turbulent boundary layer interaction results in a fully elliptic mathematical formulation which precludes analytical solution without extensive simplification.

Inger and Mason (Refs 10, 11, and 15) have extensively studied shock-boundary layer interactions analytically. The analytical approach is very instructive in providing trends, physical understanding of experimental data and numerical results. Melnick and Grossman (Ref 17) also studied weak interactions with an asymptotic/numerical approach which is a combination of the analytical and numerical approaches. However, it is still limited by simplifying assumptions to the weak interaction case. At the present time no analytical method exists capable of predicting the flow field when separation occurs, even though some analytical techniques are efficient for the calculation of some critical characteristics of the problem (Ref 18). These methods may provide the conditions for initial separation, but they have little hope of predicting the extent of separation effects and would likely over-restrict any design process.

As noted by Green (Ref 9) the coupled region of the flow which may be regarded as "interaction", is more extensive when the shock is normal. The mixture of supersonic flow, subsonic flow, viscous boundary layer, vortex sheet, strong normal shock, weak oblique shocks, and possible separation and reattachment are all exhibited by the normal-shock interaction problem. Although in the late 1940's and 1950's, extensive experimental effort (Refs 2, 8, 13 and 19) concentrated on shock induced separation; the first detailed quantitative work for a strong normal-shock turbulent boundary layer interaction was done by Seddon. Figure 2 illustrates the strong normal-shock turbulent boundary layer interaction as documented by Seddon (Ref 24) and has become the accepted structure for such interactions. Recent experimental efforts (Ref 1, 7, 12, and 16) have added to the base of understanding of such interactions. The inherent problems of conducting experimental research at near sonic conditions have limited the experimental results to relatively few measurements on only basic geometries. The introduction of very small probes into the flow at near sonic conditions often results in marked alteration of the flow. Therefore, the flow field measured very frequently does not represent the desired phenomenon. Most experimental efforts are conducted in closed wind tunnel test sections where shock interactions with boundary layers on side walls, floor, and ceiling usually alter the desired flow field. In addition to the disturbance due to the probe, the solid blockage of the entire test apparatus can cause alteration of the flow. Velocity measurements can be made without introducing any apparatus into the test section by analysis of the Doppler shift in monochromatic light when back-scattered from particles in the flow. Abbiss (Ref 1) and East (Ref 7) have applied such a laser anemometer to this problem and their results will serve as the primary experimental basis for comparisons in the current study.

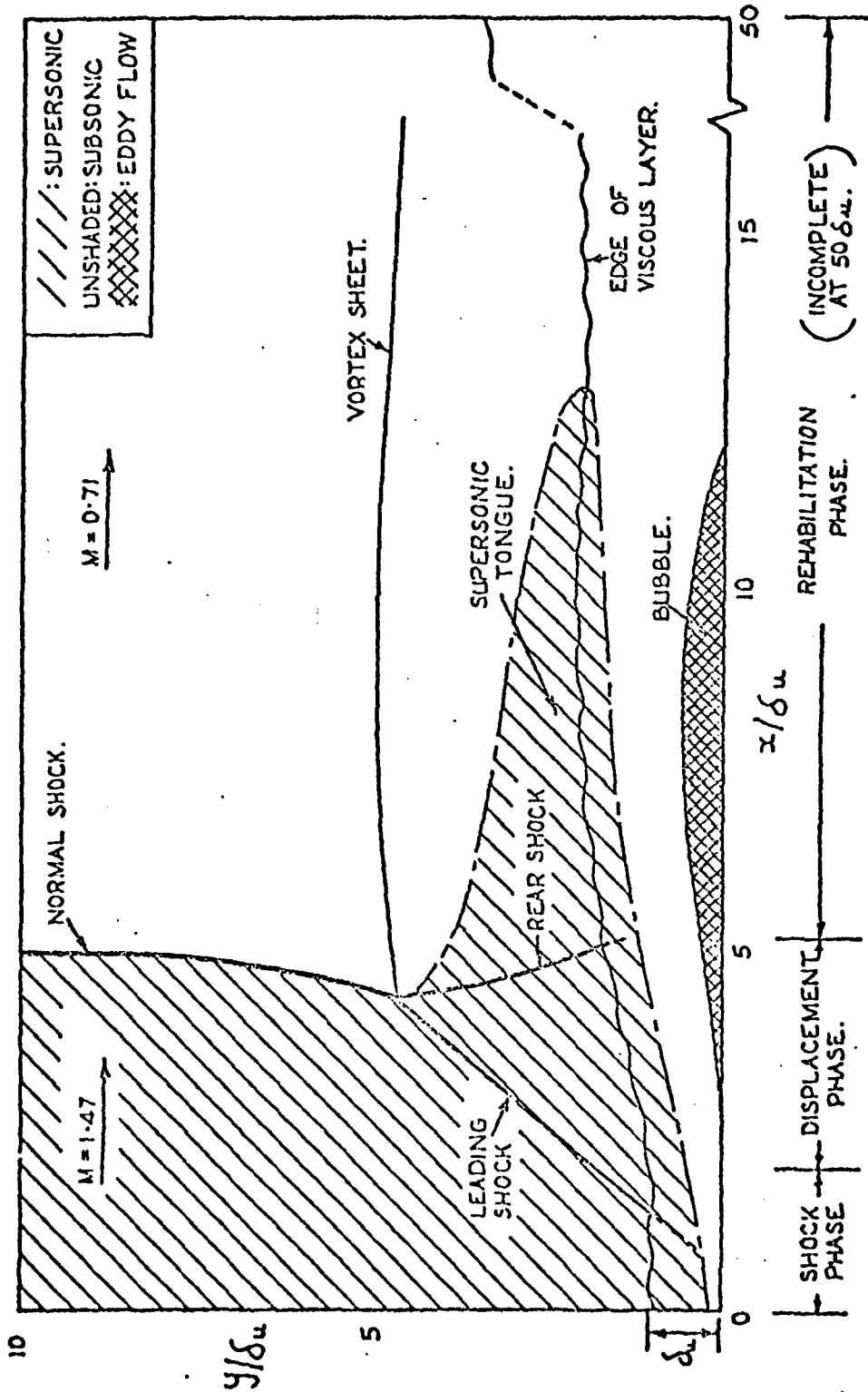


Figure 2. Seddon's Normal-Shock/Turbulent Boundary Layer Interaction Model

The third and currently most active method of investigation is numerical analysis via high speed computer. An extensive review of finite difference methods in computational fluid dynamics is given by Roache (Ref 21). Numerical methods are presently being applied to many previously unsolvable problems in fluid mechanics. For this effort a finite difference scheme was chosen over finite element methods, because the current stage of finite element application to aerodynamic problems makes that approach well beyond the scope of the present study. .

Finite difference solutions to the Navier-Stokes equations by asymptotic convergence of the time dependent equations to a steady state value is a well established approach (Ref 3, 5, 6, 14, 16, 20, 21, and 25-31). Finite difference methods are explicit, implicit, or hybrid (a combination of explicit and implicit difference equations for each time step). The implicit approach has an inherent numerical stability advantage. It allows larger time steps per computational iteration, but usually requires a more complex computational procedure for each time step. An implicit approach similar to Roach (Ref 20) would be very attractive from a computational efficiency view point, but to date, no demonstrated success of such a method at high Reynolds numbers for a transonic interaction is known. The hybrid explicit-implicit finite difference method of MacCormack (Ref 14), described in Appendix A, was chosen for the current investigation because of its proven success on similar problems (Refs 6, 14, and 25-31) and the fact that the code was readily available.

Investigation Objectives

The primary objectives of this study is three fold: (1) to further validate the finite difference approach as a strong tool applicable to flows where sufficient simplifications for analytical treatment are precluded, (2) to study the numerical simulation (boundary location, boundary conditions, boundary condition implementation, and mesh size) for possible guidance to future applications of finite difference methods of this type to aerodynamic problems, and (3) to study the flow interaction problem for a better understanding of the phenomenon based on the more detailed information which numerical analysis results provide.

In summary, interactions of a normal-shock with a turbulent boundary layer have been calculated by the finite difference method of MacCormack for various flow conditions and with alternate boundary condition implementation to study both the flow field and the finite difference method and their interrelationship with each other. Specifically the flow conditions of Abbiss (Ref 1) and East (Ref 7) were duplicated and the computed solutions were compared with experimental results for both strong and weak interactions. Variation of boundary conditions, implementation method, and mesh size were performed to provide a better understanding of the solution approach. Finally, an attempt was made to understand some of the three-dimensional effects in the experimental data used for comparison.

II Approach

This numerical investigation of normal-shock turbulent boundary layer interactions was accomplished using the same basic code as Shea (Ref 28). The scheme is basically the hybrid implicit-explicit finite difference method of MacCormack (Ref 14), applied to the time-dependent two-dimensional Navier-Stokes equations (see Appendix A). Boundary conditions and their implementation constituted a major portion of the effort in this investigation. First a base line case was established, then the investigation proceeded to include varying Mach number, boundary placement, and mesh size refinement with a common boundary condition formulation. Finally, three-dimensional effects were addressed to a limited extent in an attempt to improve the comparisons of computation with experiment.

Base Line Case

The first task of the investigation was to obtain a converged solution for the reference or base line case. The flow conditions of Ref 1, freestream Mach number of 1.51 and Reynolds number of 30×10^6 per ft, were chosen. The approach was to establish a single reference case and make primary comparisons with experiment for that base line case. Then related studies, deviating from the base line case, were compared with the base line results to evaluate the effect of the change. A review of the criterion for the Ref 1 data being chosen as the base line case was presented. Then a review of the computational approach used to compute the base line case was followed by an outline of the other studies and comparisons to the base line case.

The data of Seddon (Ref 24), which were obtained on a flat plate mounted in a transonic test section, was the basis for the experimental

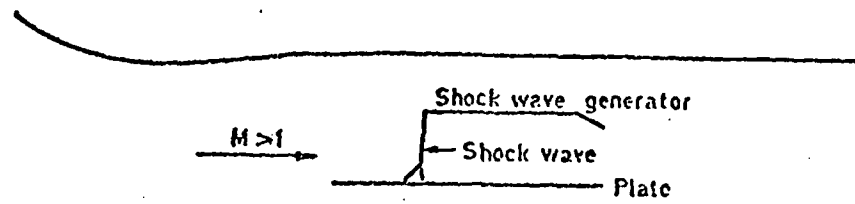
comparisons of Shea. The shock was generated by a second plate with a flap mounted above and downstream of the flat plate leading edge (see Figure 3a). The effect of the shock generator on the downstream portion of the interaction region and the unknown boundary layer characteristics on the side walls probably affect the flow field in ways that are difficult to predict. The flat plate was relatively short with the primary measuring station approximately 9 inches from the leading edge. Thus, the boundary layer thickness at the interaction was approximately 0.16 inches (Ref 28:5-6). On the other hand, the Abbiss data (Ref 1) was collected by a configuration where the shock was generated across the entire test section by a variable nozzle in the tunnel diffuser (see Figure 3b). The interaction generated by this configuration has the following inherent advantages over the Seddon data:

- a) The boundary layer is approximately 1.6 inches thick, 10 times the Seddon test, at the interaction zone.
- b) The shock generator is far downstream and should not effect the interaction region.
- c) The boundary layer should be very similar on all four walls, therefore, the effects should be symmetrical and more predictable.

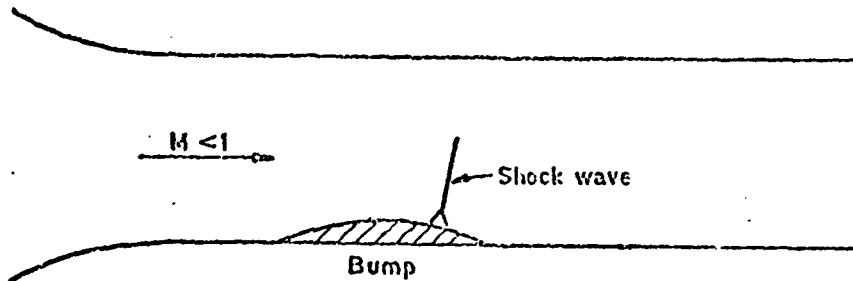
Data produced by tests (Ref 4) incorporating a wall bump to produce the shock wave (Figure 3c) were not selected. The unsymmetric test section configuration and pressure gradients downstream of the shock would introduce undesired complications to the flow field.

The laser anemometer, which was the primary means of data acquisition for both Abbiss and East, does not introduce any probes or support mechanisms into the test section. Therefore, the likelihood of altering the flow field by the measuring devices was almost totally eliminated.

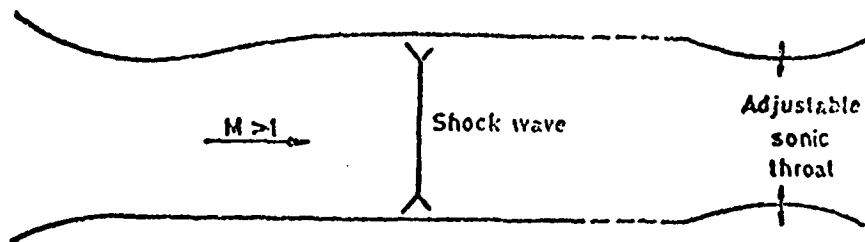
The Mach 1.51 case was chosen as the base line case because no previous comparisons to these data are known, the test approach provides a



a. Seddon's Test Configuration (Ref 24)



b. Altstatt's Test Configuration (Ref 4)



c. Abbiss (Ref 1) and East's (Ref 7) Test Configuration

Figure 3. Normal-Shock/Turbulent Boundary Layer Interaction
Experimental Configurations

flow field which should be more symmetric than the other known data, there are more data available for this case than for any others with this test configuration, and the data acquisition approach is expected to have no effect on the flow field. The Mach 1.51 flow is very comparable to the results of Seddon and Shea ($M = 1.47$) which can be used to provide additional information and understanding. With the flow conditions and finite difference approach established, attention was focused on establishing the computational mesh structure and boundary conditions and then obtaining a converged solution for the base line conditions.

The computational domain was extended in the y direction to 1.5 ft from the wall compared to 1.33 ft by Shea (Ref 29). This extended outer edge of the computational domain is geometrically at the same distance from the wall as the wind tunnel center line. Thus, the computational domain is bounded by a plane of symmetry and a flat wall. The boundary conditions for the base line case are presented here for the five regions shown in Figure 4.

Wall Boundary. The wall boundary is prescribed after Shea (Ref 28).

The boundary conditions are:

No slip wall

$$u = v = 0 \quad \text{II-1}$$

Adiabatic wall

$$(T)_y = 0 \quad \text{II-2}$$

The compatible condition of the normal (y) momentum equation at the wall yields (Ref 26) a balance of the pressure and shear gradients at the surface.

$$(p)_y = (\mu(u)_y)_x + (4/3 \mu(v)_y)_y - (2/3 \mu(u)_x)_y \quad \text{II-3}$$

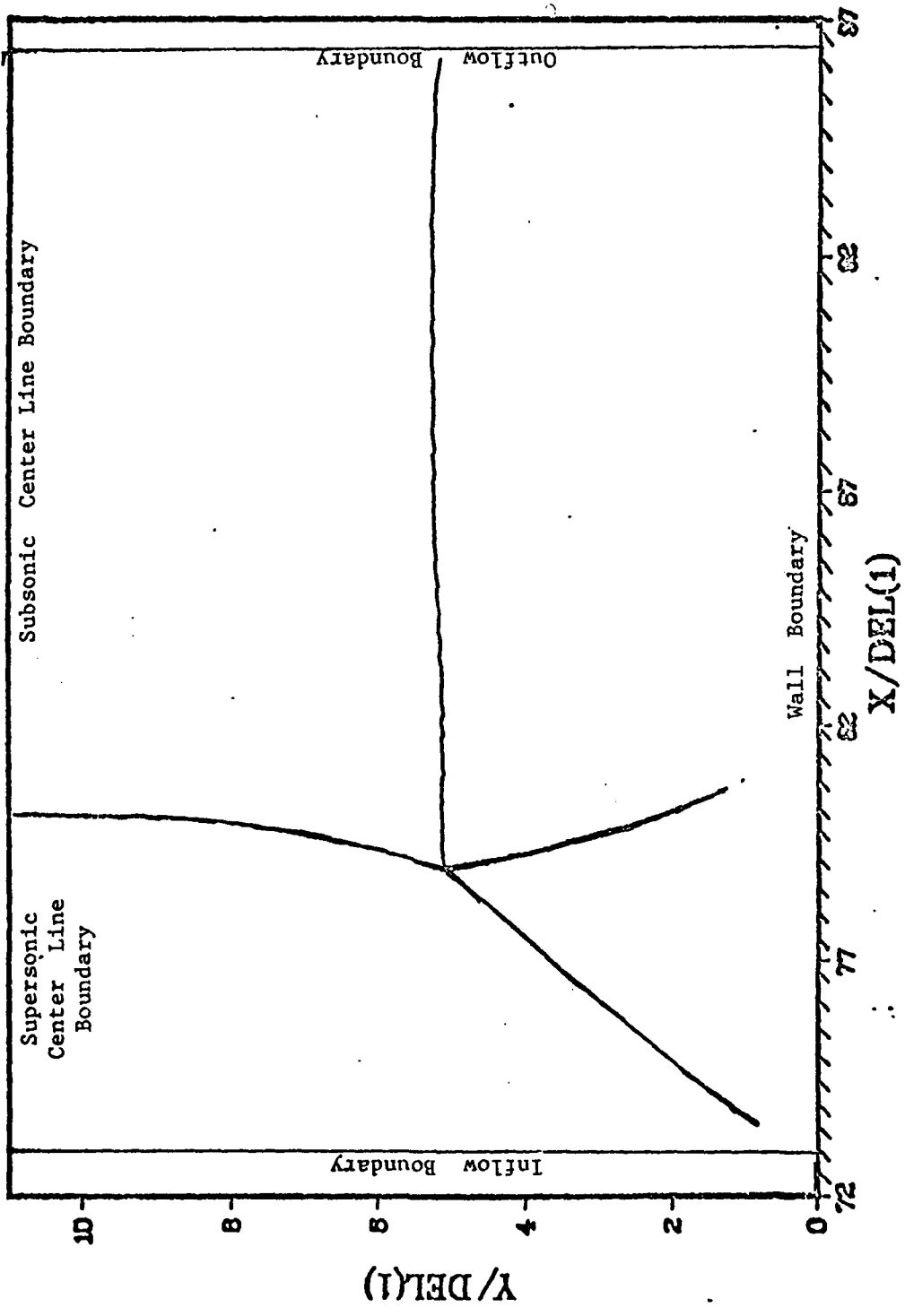


Figure 4. Boundary Condition Region Definitions

The boundary conditions were implemented by a reflection scheme where the first two rows ($J = 1$ and $J = 2$) of mesh points are equal equidistant from the wall on opposite sides. The $J = 1$ row is, therefore, positioned outside the flow field and given values which would result in the desired values at the surface by linear interpolation. The resulting finite difference expressions are presented in Appendix B.

Inflow Boundary. The inflow boundary values are from a finite difference boundary layer code developed by Shang and documented by Beauregard (Ref 5). The values for u , v , ρ , and p for all $I = 1$ (inflow boundary) mesh points were interpolated from the output of the boundary layer code. These values are held fixed.

Supersonic Center Line Boundary. The supersonic portion of the center line boundary is also in a fully supersonic region and the input is held constant with the same value as the center line point on the inflow boundary. No changes were made relative to Shea for the wall, inflow, or supersonic center line boundary treatment.

Subsonic Center Line Boundary. The upper subsonic boundary based on the new center line condition results in a formulation quite different from that of Shea. The symmetry condition at the upper boundary provides a number of possible boundary conditions. All derivatives of state properties with respect to spatial variable perpendicular to the line of symmetry (y) are zero.

$$(p)_y = (\rho)_y = (e_1)_y = (e_t)_y = (T)_y = 0 \quad \text{II-4}$$

The variation in y of all vector quantities are odd functions for vector components perpendicular to the center line:

$$v(y) = -v(-y) \quad \text{II-5}$$

where y is measured from the center line. Similarly, the variation in

y of all vector quantities are even functions for vector components parallel to the center line;

$$u(y) = u(-y) \quad \text{II-6}$$

thus

$$(u)_y = v = 0 \quad \text{II-7}$$

If the flow at the center line is also assumed to be inviscid and adiabatic, the steady state solution can be shown (see Appendix B) to require that

$$(e_t)_x = 0 \quad \text{II-8}$$

Several boundary condition formulations are therefore possible for the center line boundary. The base line case was computed with

$$v = (u)_y = (\rho)_y = (p)_y = 0 \quad \text{II-9}$$

The implementation of the center line boundary derivative quantities is by a two-point first-order extrapolation. Letting Z be a typical variable (see Appendix B)

$$Z(I, JL) = \frac{Z(I, JLM1) + Z(I, JLM2)}{2} \quad \text{II-10}$$

Which gives a value of u, ρ , and p on the subsonic center line which is an average of the two points just below it. Alternate formulations of the center line boundary conditions and their implementation will be discussed in Section III.

Outflow Boundary. The outflow boundary has been found to be rather important. The base line case was computed using an assumption that the outflow boundary is far enough downstream that the primitive variables (ρ , u, v, and p) are nearly invariant. The no-change condition is commonly used for MacCormack's scheme to minimize the upstream influence (Ref 14, 26).

$$(\rho)_x = (u)_x = (v)_x = (p)_x = 0 \quad \text{II-11}$$

These conditions were implemented by a one-point first-order extrapolation

Again, letting Z be a typical variable

$$Z(IL, J) = Z(ILM1, J)$$

II-12

for all J . Discussion of alternate formulations of the outflow boundary is provided in Section III.

Other Studies

Two other investigations were conducted. They were variation of outflow boundary position and variation of free stream Mach number.

Outflow Boundary Position. After the base line case was established, variation of the outflow boundary position was investigated. The outflow boundary was located at three alternate positions. The base line location of the outflow boundary is approximately 18 times the undisturbed boundary layer thickness downstream of the shock location. The first alternate position was half way between the base line position and the shock wave or approximately 9 boundary layer thicknesses downstream from the shock. Next, the outflow boundary was placed midway between the first two cases or approximately 13 to 14 boundary layer thicknesses behind the shock location. The streamwise mesh spacing was the same for both of these forward locations as it was for the base line case. Because of convergence problems with both of the cases for outflow boundaries forward of the base line case, a third case was computed.

The third alternate outflow boundary position was approximately 29 boundary layer thicknesses from the shock location. This location was obtained by increasing the streamwise mesh spacing by 50 percent. No attempt was made to run a smaller mesh size because of time constraints and computer memory limitations with the larger number of mesh points required.

Mach Number Variation

In addition to the base line case ($M_{\infty} = 1.51$) cases for $M_{\infty} = 1.3$ and $M_{\infty} = 1.4$ forward of the normal shock were also computed. These cases were calculated using the same boundary conditions as for the base line case. The results of these simulations are compared with the experimental results of East (Ref 7) in the next section.

III Discussion and Results

The computed base line case, $M_\infty = 1.51$, was compared with the experimental data of Abbiss (Ref 1). Several alternate boundary condition formulations were computed and compared with both base line computation and the Abbiss experimental data. Computations were also performed for $M_\infty = 1.30$ and $M_\infty = 1.40$ with the same boundary condition formulation as the base line case, and these results were compared with the experimental results of East (Ref 7). The East results were obtained in a subsequent test in the same facility as that of Abbiss with only minor modifications to the experimental approach. Since separation is inherently a three-dimensional phenomenon, three-dimensional effects were discussed. Results from an attempt to correct the two-dimensional numerical method for the most significant three-dimensional effects were presented and compared with the computations of Shea (Ref 29).

Identification of Results. An identification code was assigned to each case since several different cases were computed. Table 1 gives a complete list of identification codes and a corresponding description of each series of computations. The alphabetic part of the code identifies the flow conditions and boundary condition formulation with respect to the base line case. The numerical portion of the identification indicates subsequent iteration of the solution. The higher numbers are later runs. Typically, the solutions were advanced 120 time steps for a total elapsed time of approximately 0.002 to 0.0025 seconds between data sets. Table 1 is provided as a guide to the identification of the data source for data plots in this section.

Solution Convergence. A convergence criterion was established and applied as follows. The wall surface pressure distribution was plotted

Table I

Computation Code ID Key

SERIES ID CODE	Description and Remarks	
O	Base Line Case, See Section II For Description CLBC ¹ $v = (\rho)_y = (u)_y = (p)_y = 0$ Type ³ 1 OFBC ² $(\rho)_x = (\rho u)_x = (\rho v)_x = (e_t)_x = 0$ Type 2	
H	CLBC $v = (\rho)_y = (u)_y = (p)_y = 0$ Type 3 OFBC $(u)_{xx} = (v)_{xx} = (p)_{xx} = (\rho)_{xx} = 0$ Type 4	
J	CLBC All Values Fixed at Normal-Shock Values OFBC Same as H-Series	
K	CLBC Same as H-Series OFBC Same as O-Series	
L	CLBC $v = (\rho)_y = (\rho u)_y = (H_t)_x = 0$ ofbc Same as O-Series	
M	CLBC Same as H Except Type 5 OFBC Same as O-Series	
N	CLBC $v = (\rho)_y = (H_t)_x - (\rho u)_x = 0$ OFBC Same as O-Series	
P	All Boundary Conditions Same as O-Series IL = 40 (IL - 64 for all previous cases)	

Table I (cont'd)

R	All Boundary Conditions Same as O-Series IL = 52	
S	Same as O-Series Except $Dx = 0.778$ (50% increase from value for all other Series)	
Q	All Boundary Condition Same as O-Series $M_\infty = 1.30$	
V	Boundary Conditions Same as O-Series $M_\infty = 1.40$	
B	See Reference 28 (B-Series Constitutes Ref 29)	
I	All Boundary Conditions Same as O-Series JL = 22 (JL = 32 All other runs except U-Series)	
T	Same as O-Series	<u>Except:</u> $\sum_{J=1}^{JL} \rho u(J) DY(J) \quad \left \begin{array}{l} I = 1 \end{array} \right.$
U	Same as I-Series	$= \sum_{J=1}^{JL} \rho u(J) DY(J) \quad \left \begin{array}{l} I = IL \end{array} \right.$

1. Subsonic Center Line Boundary Conditions
2. Outflow Boundary Conditions
3. See Table 2 for description of difference equation types

Table II

Difference Equation Type Definition

Type	Definition
1	$Z(JL) = (Z(JLM1) + Z(JLM2))/2.0$
2	$Z(IL) = Z(ILM1)$
3	$Z(JL) = Z(JLM1)$
4	$Z(IL) = 2.0 * Z(ILM1) - Z(ILM2)$
5	$Z(JL) = (4.0 * Z(JLM1) - Z(JLM2))/3.0$

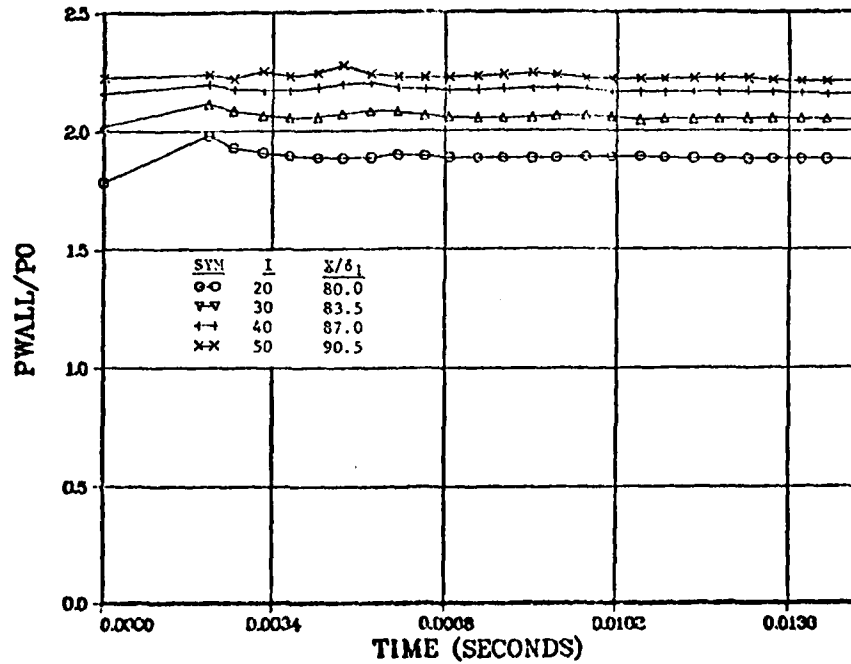


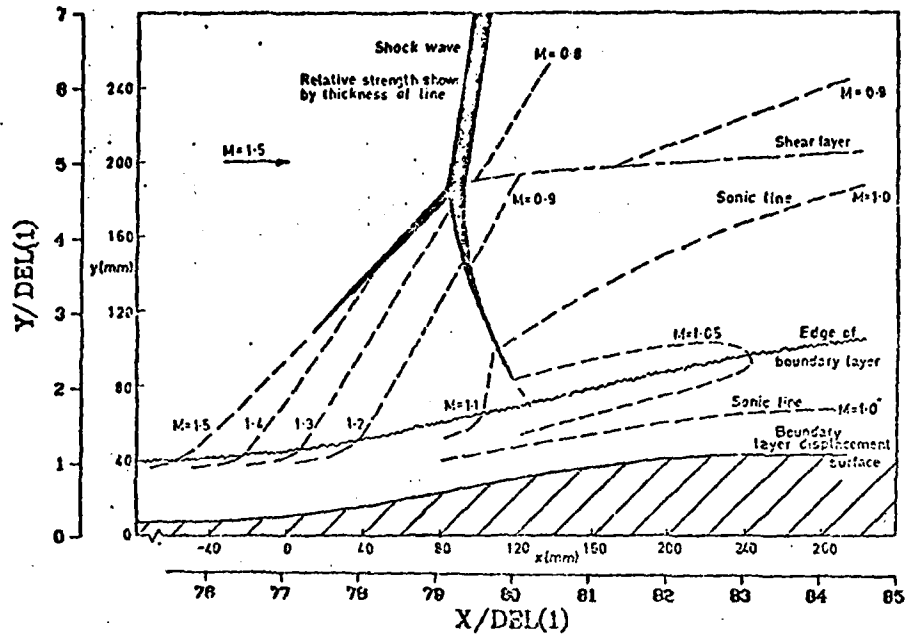
Figure 5. Base Line Case (O-Series) Convergence Plot

every 30 time steps. When the wall pressure ratios remained constant, did not change by more than 0.01 (0.3 → 0.8%) in a characteristic time (approximately 180 time steps), convergence was said to be established. With an expected accuracy of the experimental data no better than 1% and the expected comparison between computation and experiment approximately 5 to 10%, the 0.01 criterion represents an attainable resolution which should not introduce scatter into the results of this study. Early in the investigation, complete longitudinal distributions were plotted for sequential data sets. It was concluded that the pressure variation of selected locations plotted verses time gave a good representation of the steady state asymptote. Figure 5 is the convergence criterion plot for the base line (0 Series) results. It is a typical result and any deviation from this type of plot will be discussed.

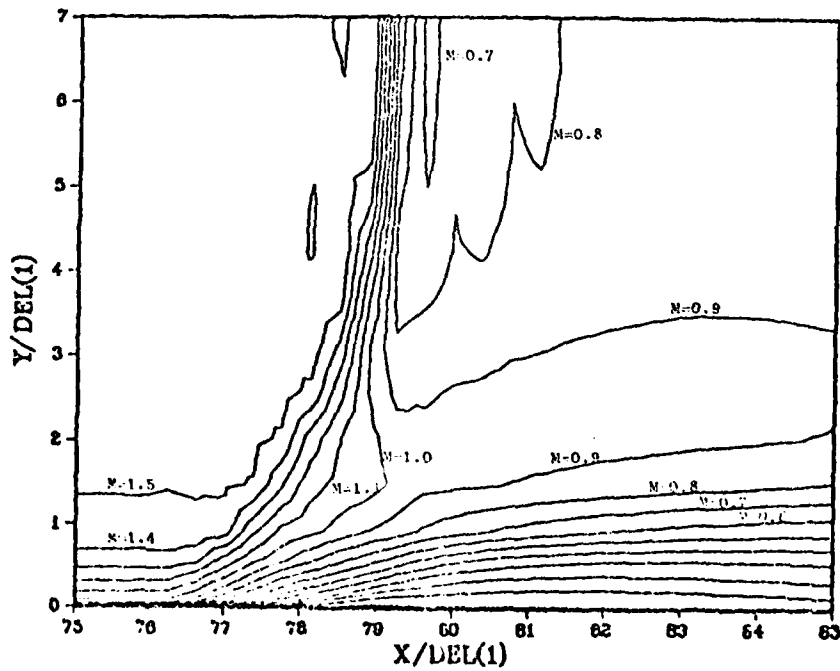
The results presented herein were obtained using the (Wright-Patterson AFB, ASD) Cyber 175 computer. Computations required approximately 15 minutes per characteristic time. Thus, 60 to 75 minutes were required to obtain a converged solution with a boundary condition formulation similar to the base line case.

Base Line Case Results

The numerical and experimental (Ref 1) results show qualitative agreement as can be seen in Figure 6. The lambda shock structure can clearly be seen in the computed Mach contours of Figure 6b. The boundary layer exhibits rapid growth and a series of compression waves are generated in the supersonic flow. Although these compression waves do not form a distinct bifurcation point, they are collimated into a single longitudinal mesh space at approximately the same height as the experimentally determined bifurcation point. The shear layer which is shed



a. Abbiss (Ref 1) Data Mach Contours



b. Data Set 07 (Base Line Case) Mach Contours

Figure 6. Experimental and Numerical Mach Contours for Base Line Case

from the bifurcation point is not observed in the numerical results because the mesh spacing is too coarse in that region.

The Abbiss results do not provide the details of the boundary layer in the interaction region because of measurement difficulties close to the wind tunnel wall. Seddon (Ref 24), however, shows that for $M_\infty = 1.47$ the separation bubble length is approximately 12 times the undisturbed boundary layer thickness which agrees with the computed results. The computations and Seddon both show a smooth pressure distribution in the reattachment region. The maximum separation bubble height and the location of the maximum height of separation in the Seddon data and the present numerical results are quite different. Seddon's results show a maximum separation bubble height of about half the initial boundary layer thickness compared to approximately 0.1 the initial thickness height for the computations. Seddon measured the maximum height at 70% of the bubble length compared to a 40% location for the computed results. The poor agreement should not be unexpected. Since the separation bubble size and structure is likely a strong function of the post shock pressure distribution, and the post shock pressure distribution is probably affected by the differences between the Seddon experimental arrangement and the numerically simulated problem which is based on the Abbiss test configuration. In addition, the turbulence model was an algebraic mixing length model developed for primary application to attached turbulent boundary layers in equilibrium. Although the use of this model (Ref 28) and similar models (Refs 5, 6, 14, 16, 25-31) is common practice, they should not be expected to model the detailed separation structure. Viegas et al (Refs 6, 30, 31) have studied more complex turbulence models extensively with mixed results. Further, separation and turbulence are inherently a three-dimensional phenomena and detailed modeling cannot be accomplished by a two-dimensional analysis.

The most obvious disagreement which can be observed in Figure 6 is the total lack of a post shock supersonic region, commonly called the supersonic tongue. Three possible explanations for this discrepancy are offered. First, the mesh structure is quite coarse in the region where the supersonic tongue is thought to exist and the resolution may not be sufficient to exhibit the required detail to describe the supersonic region. Second, the supersonic region is quite possibly a product of a three-dimensional blockage effect produced by the rapid boundary layer growth on all four walls of the post shock region of the interaction. Finally, the data reduction technique assumed constant static pressure in the boundary layer from which local Mach numbers were calculated. The computed local flow variables in the post shock boundary layer region are not constant. The differences are of sufficient magnitude to produce local Mach numbers of slightly less than $M = 1.0$ in the post shock outer boundary layer edge region. It should also be noted that measurements in this region required that the optics pass through the strong interaction region of the tunnel side walls and that the Seddon model was used by Abbiss as a guide for his experimental effort. Also, no evidence of post shock supersonic flow can be discerned from the Schlieren data in the Seddon results.

A more quantitative comparison of the base line computation with the Abbiss data is presented in Figures 7 and 8. As will be discussed further in a later section, the shock could not be positioned exactly in a given longitudinal location by the shock implementation procedure used for the computations. Although the relative location of the shock varied less than one undisturbed boundary layer thickness (not enough to affect the interaction) from the established reference location for most cases computed, it would cause unrealistic scatter in the results if not resolved

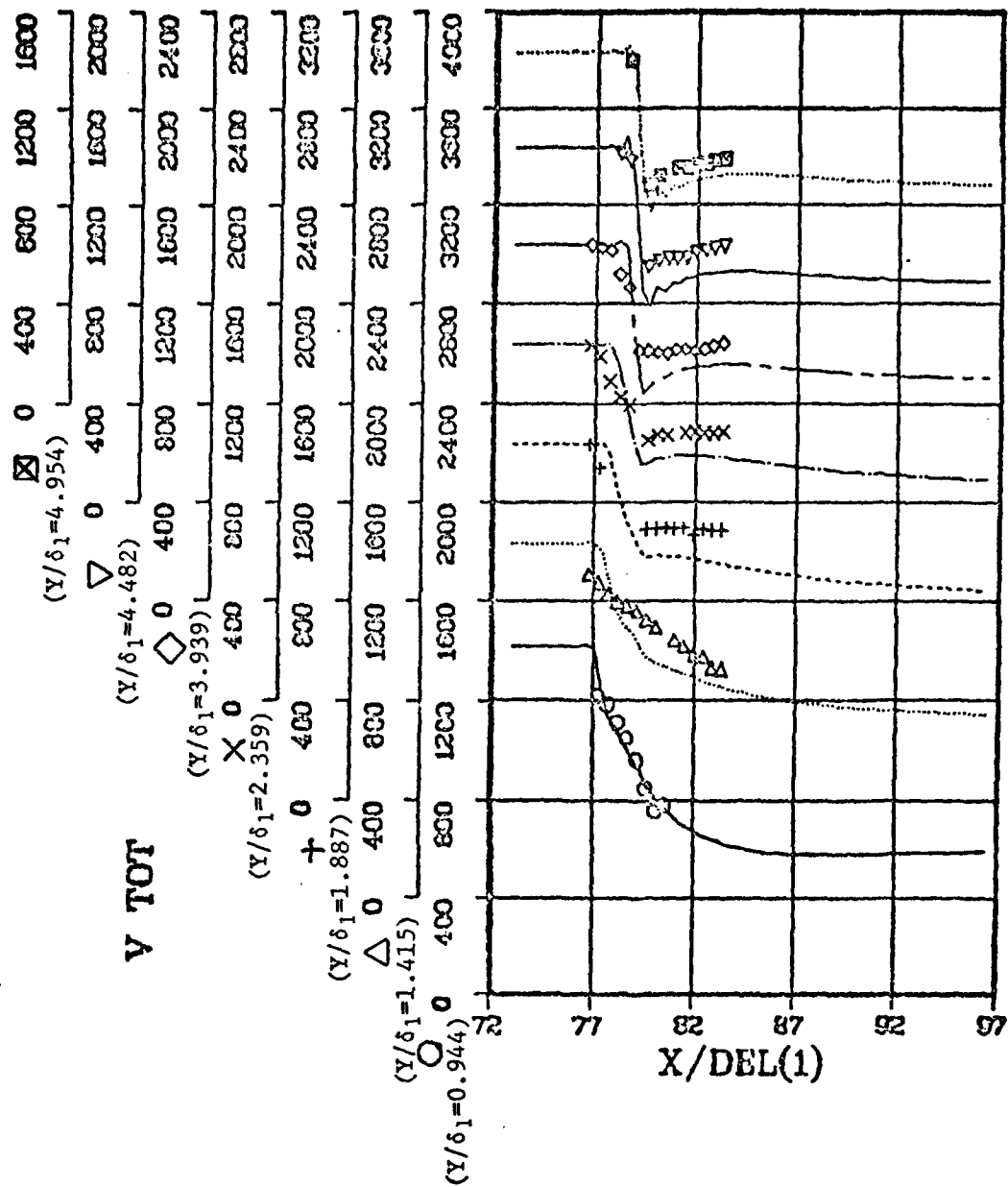


Figure 7. Base Line Case Experimental and Numerical Longitudinal Total Velocity Profiles

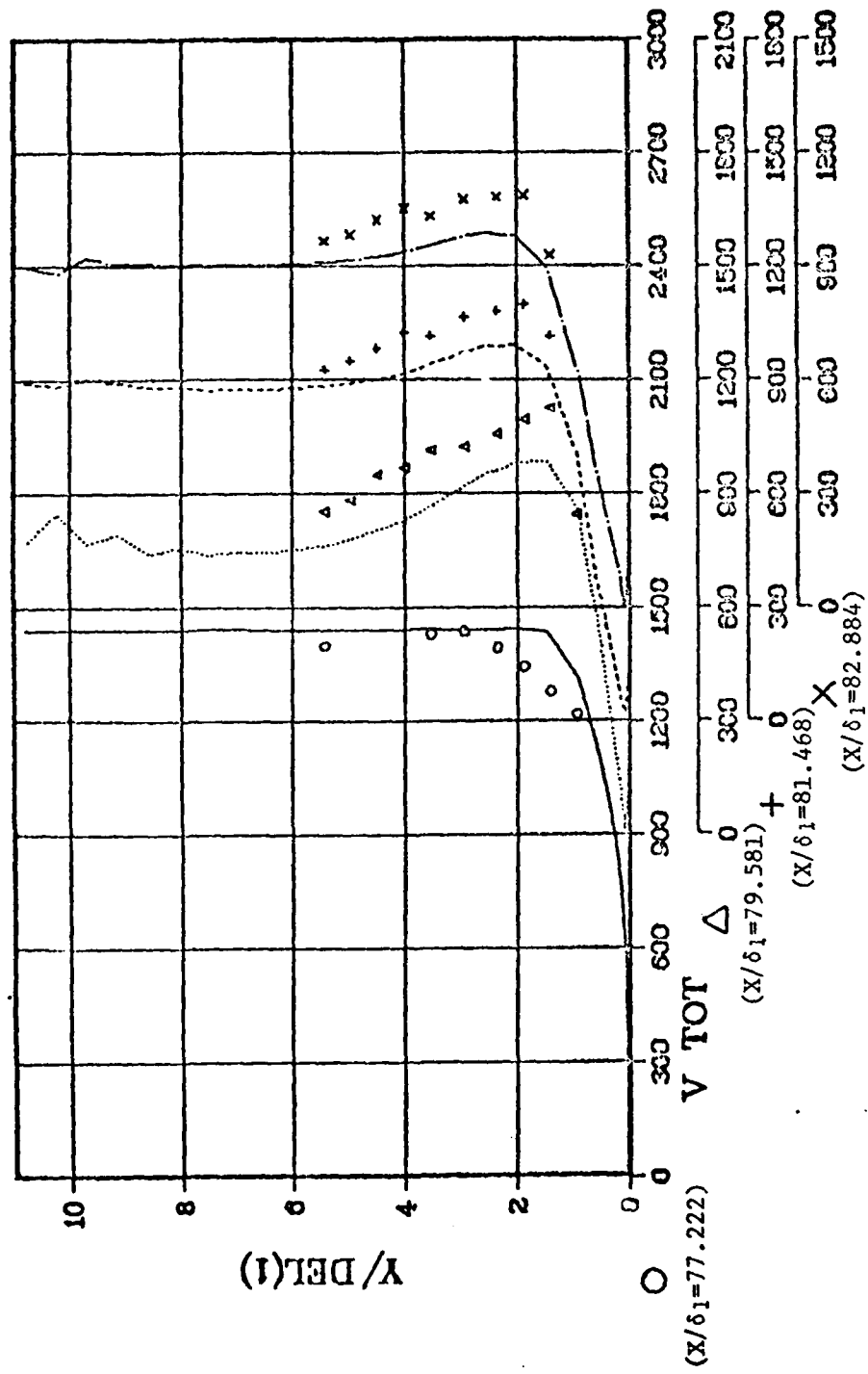


Figure 8. Base Line Case Experimental and Numerical Transverse Total Velocity Profiles

prior to plotting. For one profile where the shock jump was distinctive with respect to x-location ($y/\delta_1 \approx 4.954$) the effective x-location was adjusted for all computed and measured results. This relative location was then held fixed for all subsequent plotting.

The comparison of longitudinal profiles (Fig 7) shows practically all points are within 10% of the measured values. The agreement is excellent for the $y/\delta_1 = 0.944$ curve which is closest to the wall. The superior agreement for this profile is attributed to the refined mesh in this region and the reduction of three-dimensional effects due to the proximity of the wall.

The experimental velocities are consistently higher in the subsonic regions of the flow. The velocity decrease across the shock is approximately 100 ft/sec less for the experimental results relative to the calculated values. The shock jump when predicted by the one-dimensional Rankine-Hugoniot relations yields a post shock value of 766 ft/sec. If instead of a normal-shock an 81 deg oblique shock jump is computed, the results agree well with the measured data and an 85 deg oblique shock jump agrees with the computed results. Therefore, the differences noted between the measured and computed results can be accounted for by small differences in the shock angles relative to the local flow in the supersonic regions. This explanation would also account for the much better agreement in the single subsonic profile ($y/\delta_1 = 0.944$).

The subsonic region of the profiles shows excellent agreement in shape. Relative to the calculated values, higher experimental velocities are found in the supersonic regions and lower experimental velocities are in the subsonic region. The consistently higher supersonic velocities and lower subsonic velocities suggest the effect of an area restriction on both regions of the flow. It is concluded that the predominant difference

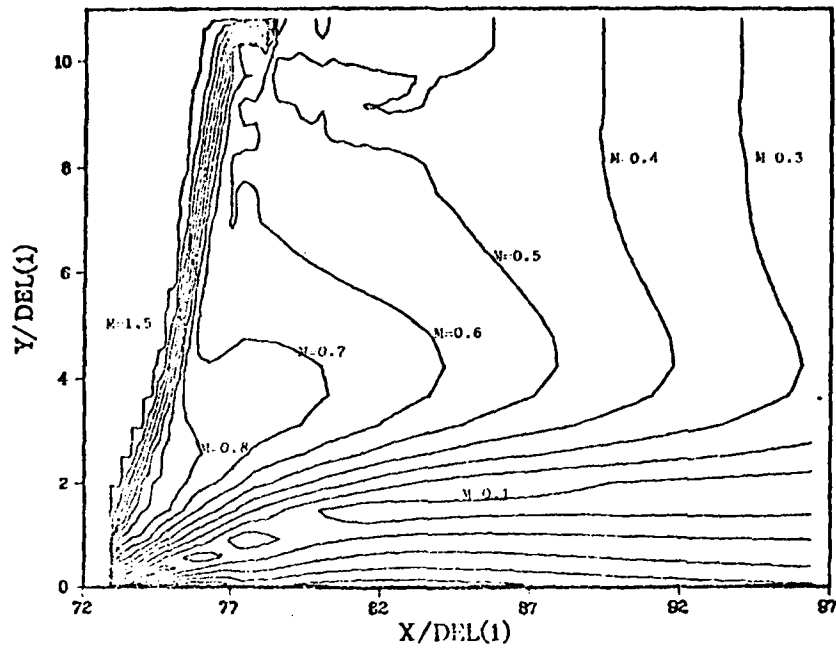
between the experimental results of Abbiss and the computed results is the three-dimensional area restriction imposed on the flow by the rapid expansion of the boundary layer displacement thickness on the side walls of the tunnel. This three-dimensional effect is not modeled by the two-dimensional computations reported herein.

The vertical profiles of Figure 8 present the same data in a different format and support the same conclusions. Once again the vertical profiles show qualitative agreement in shape. The additional blockage due to three-dimensional effects is also a likely cause of the higher shock angles relative to the flow direction in the experimentally measured results. Shea (Ref 28) argued that the Seddon results exhibited strong three-dimensional effects. This claim was supported by Winter (Ref 32), who indicated that the interaction region for both the Abbiss and East data are strongly three-dimensional. Winter's statement was based on oil flow and pressure data obtained in conjunction with the experimental efforts reported by Abbiss and East. While the computed results are different from the experimental data, all of the differences are consistent with the expected difference between the two-dimensional formulation of the base line case and the measured data which exhibit known three-dimensional effects. An attempt to account for these three-dimensional effects will be discussed later.

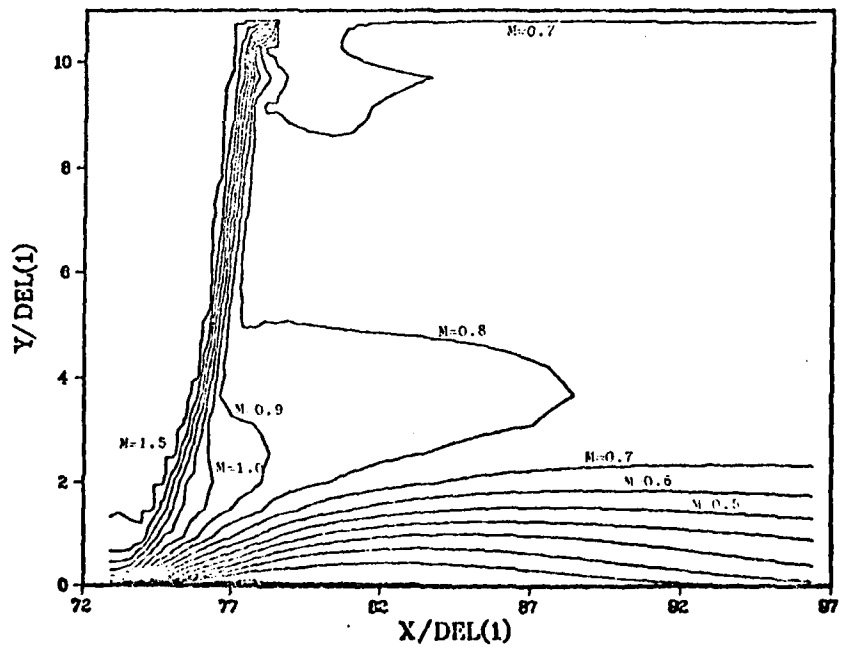
Boundary Conditions

Outflow Boundary Conditions. The early phase of the investigation concentrated almost completely on the evaluation of alternate subsonic center line boundary treatment and the outflow boundary condition was

$$(v)_{x x} = (u)_{x x} = (\rho)_{x x} = (p)_{x x} = 0 \quad \text{III-1}$$



a. Data Set H10 Mach Contours



b. Data Set J8 Mach Contours

Figure 9. Mach Contours Depicting Ill-treatment of Outflow Boundary Conditions

Figure 9a shows a Mach contour plot of the final H-series computation. The particular center line boundary treatment for this series is defined in Table I for completeness but is not pertinent here. The plot is presented as typical of all results with the second-order outflow boundary condition. The outflow pressure continued to rise until the shock wave and the interaction was crowded forward into the fixed inflow boundary and the outflow decreased to $M = 0.25$ which was also unreasonable. The outflow conditions of Eqn III-1 were recommended in Roache (Ref 21), but have been determined to be unacceptable for a subsonic outflow boundary, at least in conjunction with the MacCormack code used herein. In an attempt to understand the problem, the subsonic center line condition was fixed with the Rankine-Hugoniot normal shock values at all post shock mesh points. The J-series (Fig 9b) Mach contours resulted. A comparison, of the H and J series computations, indicated that the result of changing the center line boundary treatment was to stabilize the outflow pressure and velocity. Subsequently, the outflow boundary condition was changed to the first derivative condition.

$$(\mathbf{v})_x = (p)_x = (u)_x = (\rho)_x = 0 \quad \text{III-2}$$

No claim is intended that the boundary conditions of Eqn III-2 are the product of an exhaustive study or that they are the best treatment possible. These conditions did provide a series of solutions to converge numerically to values which agree quite well with experimental results. As was described in Section II, the outflow boundary conditions of Eqn III-2 were implemented by assigning the values on the outflow boundary the same values as those of the adjacent points just upstream. All computations presented herein except the H, J, T, and U series were computed with this simple first-order scheme applied to the primitive variables

u, v, p and ρ . Series T and U formulation and results will be discussed in the three-dimensional effects section.

Center Line Boundary Conditions. Table I, page 19, outlines in detail the center line boundary conditions of Figure 10. The subsonic center line boundary was treated by: a first-order single-point extrapolation (K-series), a two-point second-order scheme (M-series), a constant total enthalpy and momentum approach (N-series) and the two-point first-order averaging scheme of the base line (O-series). The results (Fig 11) show no discernible difference with the possible exception of the base line case for the $x/\delta_1 = 79.5$ profile. The conclusion is that any compatible formulation of the center line boundary will produce a reasonable result if combined with an appropriate outflow boundary treatment.

The base line results for the $x/\delta_1 = 79.5$ profile exhibit the only measurable difference from the other computations in Figure 10. This deviation of a single profile just aft of the shock location can be traced to the shock implementation procedure. The normal shock jump at the center line is forced to meet the Rankine-Hugoniot relations between the supersonic and subsonic regions of the center line boundary. Figure 11 presents two sequential Mach contour plots to examine the shock jump implementation at the center line boundary. The K-series was selected as typical of the early shock implementation scheme. The K7 contours in Figure 11a show only the $M = 0.8$ contour embedding the single point, fixed by the Rankine-Hugoniot relations, just downstream of the shock on the center line boundary. Less than 1.5 characteristic times later, the K9 contours of Figure 11b show both the $M = 0.8$ and 0.9 contours have passed the fixed point and a measurable downstream movement in the entire shock structure can be observed.

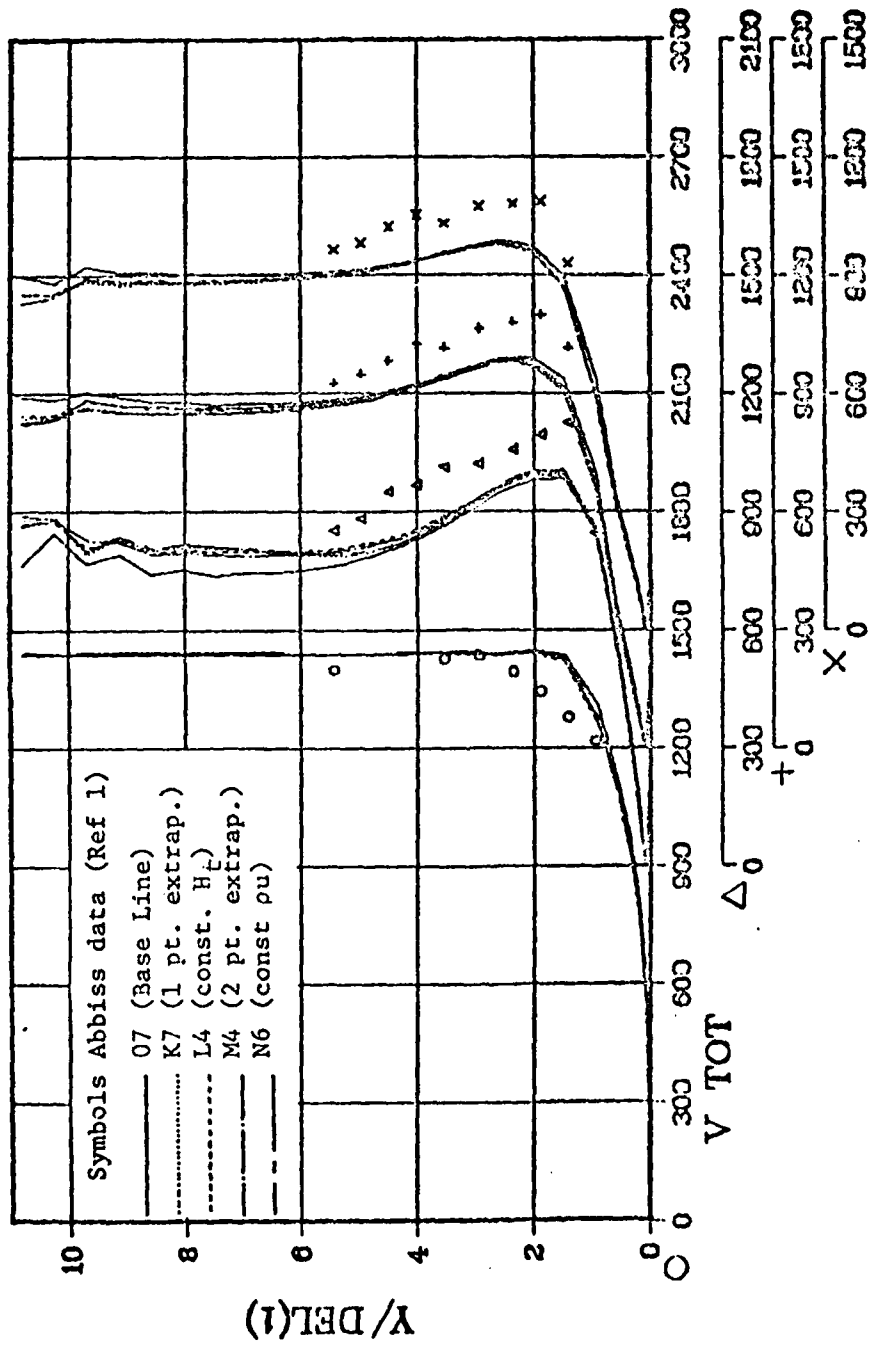
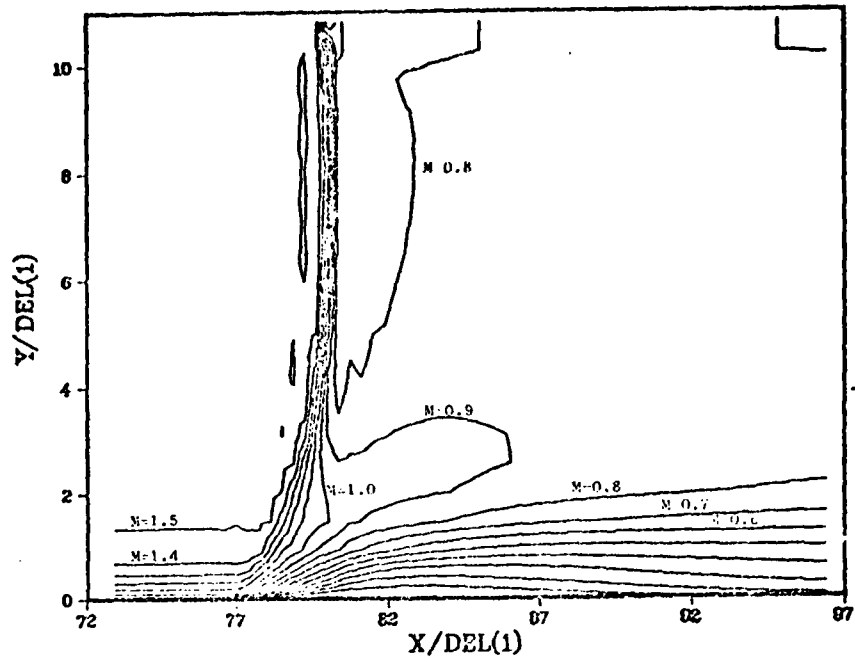
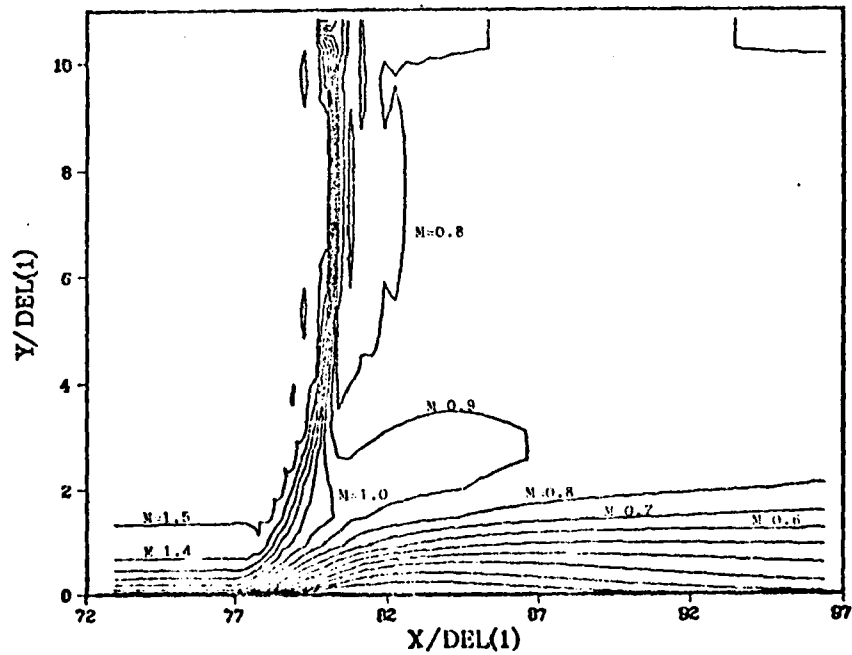


Figure 10. Transverse Total Velocity Profiles for Various Center Line Boundary Treatment



a. Data Set K7 Mach Contours



b. Data Set K9 Mach Contours

Figure 11. Mach Contours Depicting Shock Implementation Difficulty

The wall pressure ratios on the convergence plot also revealed a slow steady decrease as the shock structure moves. If allowed to continue, the entire shock will slowly bleed past the fixed point. Then the unconstrained shock wave will almost immediately pass completely out of the computational domain. In order to prevent this and to hold fixed the shock jump on the upper boundary, five consecutive points downstream of the desired shock location were assigned values computed by the Rankine-Hugoniot relations.

Several other approaches were tried. The shock was allowed the freedom to spread over 3 or 4 mesh points but it consistently formed either at the forward or rear mesh space of the allowable range. The procedure to fix five center line boundary points with the Rankine-Hugoniot post shock values was established for the base line case and used in all subsequent computations. The $x/\delta_1 = 77.2$ center line point for the base line case is in this five-point range and therefore, is artificially held at a lower value of local velocity than would otherwise be predicted. This procedure did allow the consistent convergence of the numerical method and only local effect are exhibited by Figure 10.

Outflow Boundary Location. The first-order boundary condition of Eqn III-2 was used with a common set of center line boundary conditions (same as base line case) to compute results for three alternate outflow boundary locations. The most forward location for the outflow boundary was approximately 9 times the undisturbed boundary layer thickness downstream of the shock wave. This location is denoted as the P-series and was computed at only 40 (IL=40) streamwise mesh points. The second position (denoted the R-series) placed the outflow boundary midway between the most forward position and the base line location which was

approximately 18 times the initial boundary layer thickness from the shock wave. Finally, the streamwise mesh spacing was increased by 50%, which allowed placement of the outflow boundary at approximately 29 times the undisturbed boundary thickness downstream of the shock wave without increasing the number of mesh points. Figure 12 provides a composite plot of the velocity profiles for all of these outflow boundary locations. Only the second-order outflow boundary treatment shows measurable deviation from the base line results. Since neither changes in outflow boundary location nor increased streamwise mesh spacing produce a measurable effect on the solution, it is concluded that the streamwise mesh is small enough and the outflow boundary is sufficiently far downstream that neither is a strong influence on the solution in the interaction region. A closer examination of the reattachment point and the wall shear stress values revealed that both were measurably altered by the two forward locations. Therefore, the outflow boundary should not be moved forward of the base line case without examination of potential influence on the computed results.

Mach Number Variation

The same boundary condition formulation as the base line case was used to compute the $M_\infty = 1.30$ and $M_\infty = 1.40$ cases. These cases were computed in a production manner and are compared to the East (Ref 7) results in Figure 13. The comparisons show better agreement than the Mach 1.51 case. The vertical profiles of Figure 13a show agreement within 5% to 7% and qualitative agreement in trends and shape for the corresponding curves. Once again the higher subsonic values and smaller shock jumps in the experimental data indicate measurable three-dimensional effects. The results are consistent with the separation criterion of Schlichting (Ref 22:365) which states that $M_\infty \geq 1.30$ is required to promote separation. The $M_\infty = 1.40$ case shows a small separation bubble of length approximately 4 times the

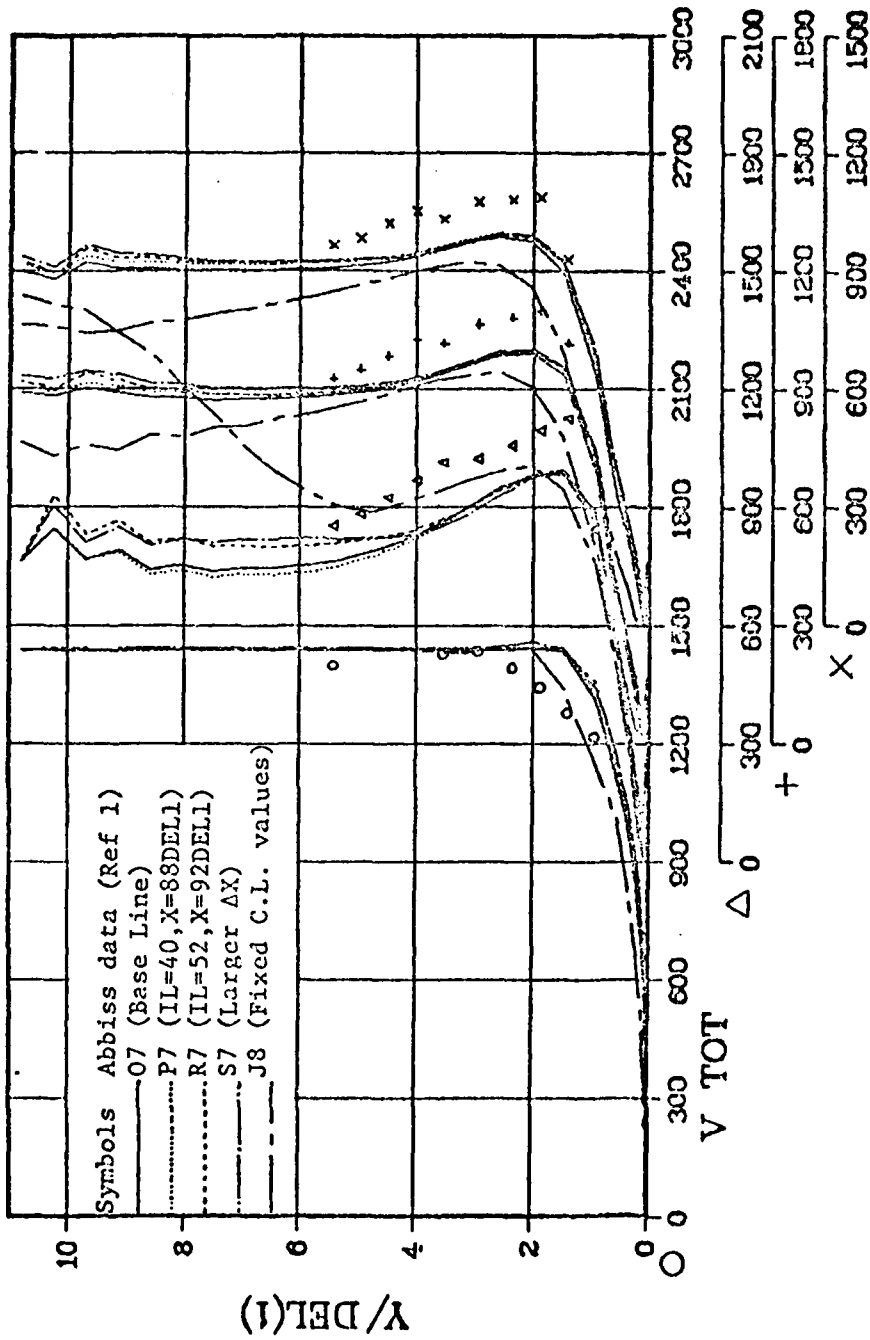
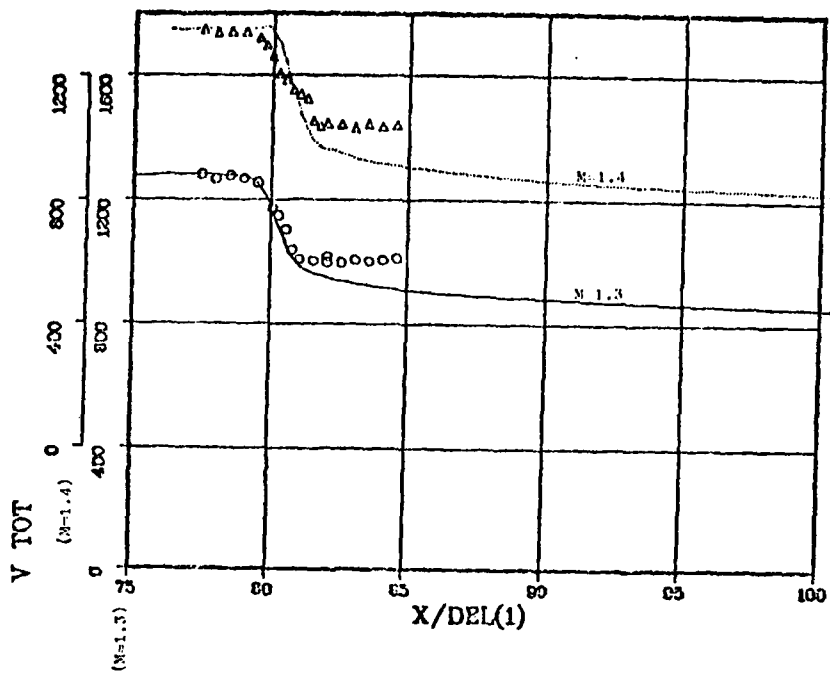
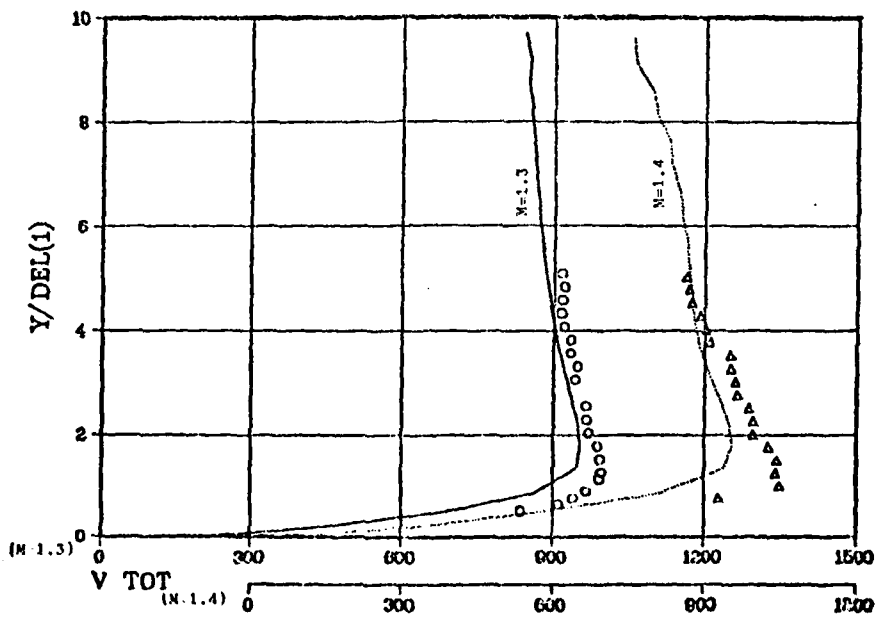


Figure 12. Transverse Total Velocity Profiles for Various Outflow Boundary Treatment



a. Longitudinal Total Velocity Profiles



b. Vertical Total Velocity Profiles

Figure 13. Mach 1.30 and 1.40 Total Velocity Profiles (Experimental and Computed)

undisturbed boundary layer thickness. The $M_\infty = 1.30$ computations had an even shorter bubble which was less than 3 times the undisturbed boundary layer thickness length with a computed maximum bubble height of 0.002 ft (less than $0.02 \delta_1$) which would be extremely difficult to observe and was obviously well into the weak interaction classification.

Three-Dimensional Effects

As was previously stated, separation is not two-dimensional and therefore inherently exhibits three-dimensional effects. The transonic character of the flow field studied caused disturbances to be perturbed across the entire duct by relatively small displacements on any of the boundaries. Shea attempted to account for the predominant three-dimensional effect by a boundary layer blockage computation which was used to determine the longitudinal ρu distribution on the subsonic region of the upper boundary. This procedure was outlined in Reference 28 and was incorporated in the Shea computations of the base line flow conditions (Ref 29). The Shea results are denoted as the B-series on Figure 14. A close examination of Figure 14 revealed that no discernible improvement over the present base line case could be seen from the Shea upper boundary treatment.

The idea of accounting for total boundary layer blockage was approached differently in the current effort. A major factor in any duct flow is to model the correct area distribution. If the area distribution is duplicated for different geometric shapes, very similar pressure distributions will be exhibited. Boundary layer methods have demonstrated the capability to calculate reasonable boundary layer characteristics by using imposed pressure distributions on a flat plate calculation to model complex geometries. An attempt was made to model the three-dimensional duct flow of

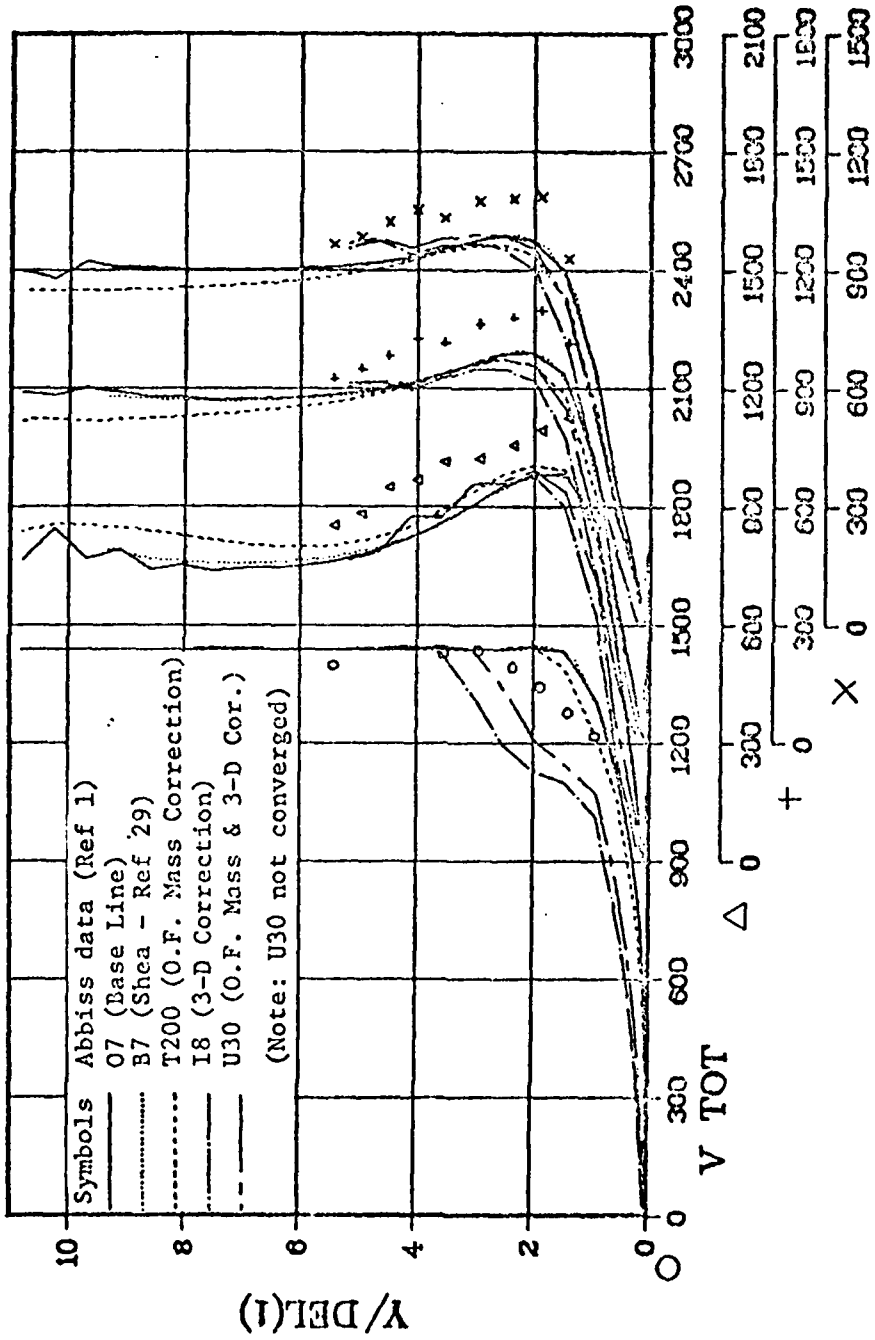
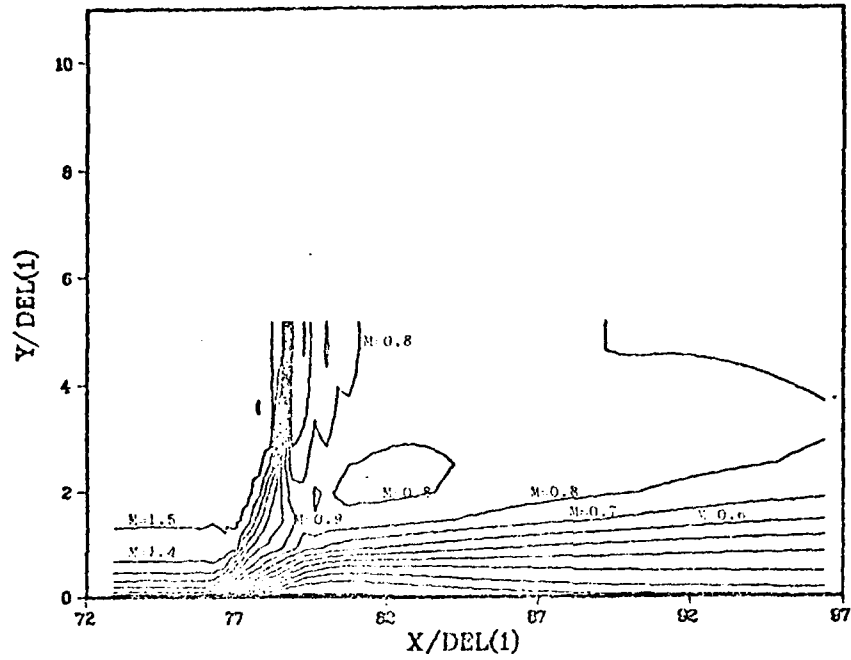


Figure 14. Transverse Total Velocity Profiles for Various Attempted Corrections

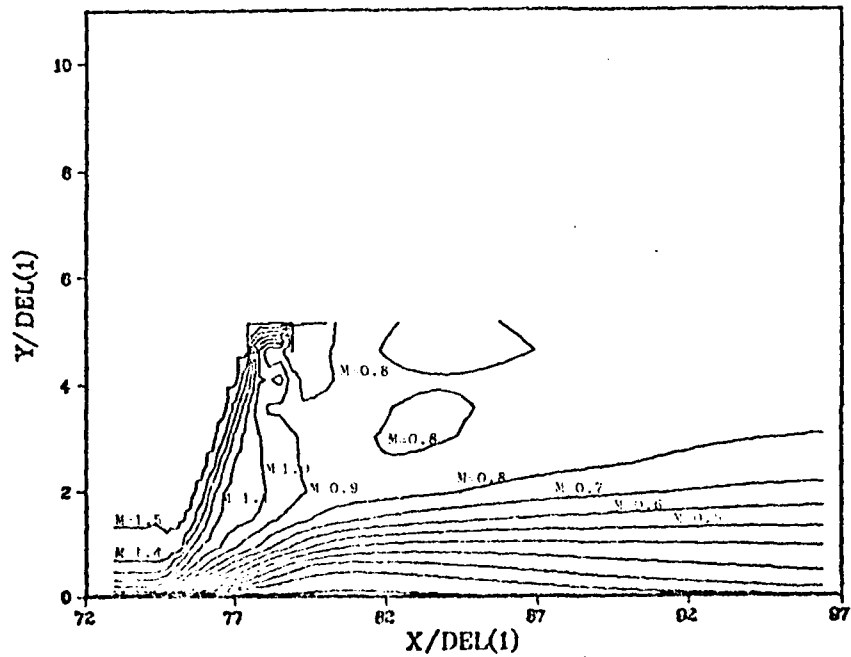
the Abbiss test by redefining the duct geometry such that the ratio of total boundary layer displacement area to total duct area was matched. This approach assumed that a two-dimensional duct with the correct blockage area ratio distribution would produce the correct pressure distribution. This pressure distribution would in turn produce a correct boundary layer displacement thickness directly in the two-dimensional calculations. Therefore, once the new duct height was computed based on the blockage area ratio, the modified duct geometry remained fixed and did not change with time. For the 3 ft x 3 ft duct of the Abbiss test and assuming negligible effects from the corners, the modified duct was assumed to be a 1.5 ft (0.75 ft to center line boundary) two-dimensional duct.

The modified duct geometry (I-series) was presented on Figure 14 as the dash-dot-dash line. The results show that the $x/\delta_1 = 79.5$ profile was over-corrected and agreement for the downstream profiles was degraded relative to the base line and experimental results. A review of Figure 15 showed that the shock has been pushed forward and was badly distorted at the upper boundary. A global check of the mass flow through each subsequent x-mesh station revealed nearly 8% apparent mass was lost (in the calculation), most of it being lost at the shock region. No conclusion about the similarity correction could be made until this large mass discrepancy was corrected.

A similar mass flow check of the base data results in an indicated 2% mass gain at the shock region. Figure 16 shows the shock for the base line case was noticeably distorted near the upper boundary. It was also obvious that the local distortion of the Mach contours (Fig 16a) was not indicative of a center line boundary. It was observed that in cases where mass was lower at the outflow boundary, the shock structure was forced forward of the desired shock location. Conversely, where the mass

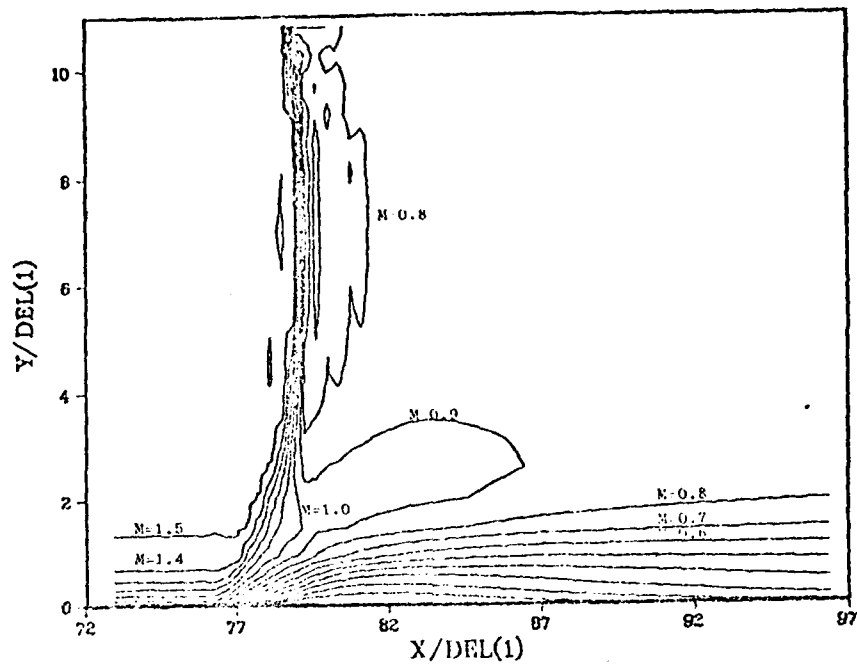


a. Data Set II Mach Countous

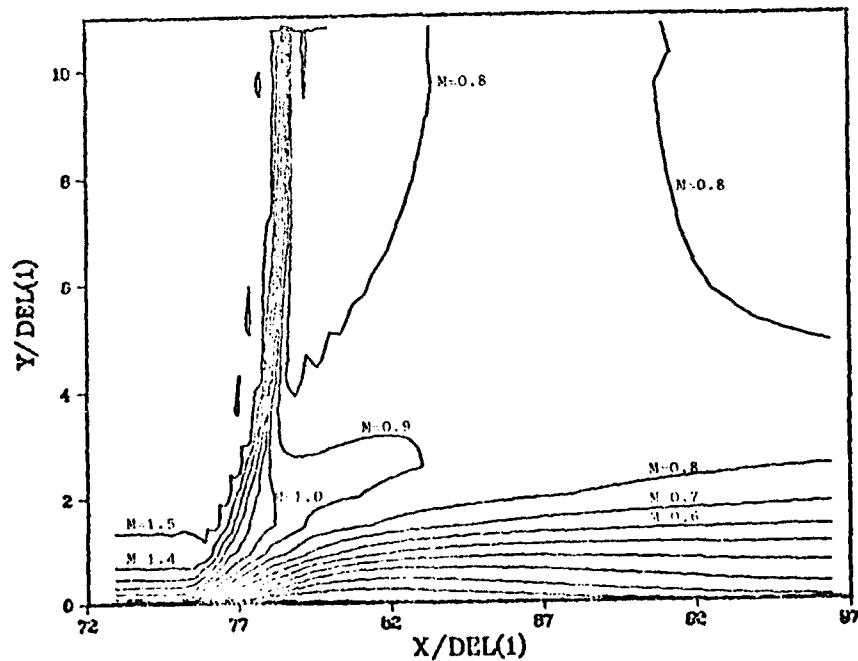


b. Data Set 18 Mach Contours

Figure 15. Mach Contour Distortion for Attempted 3-D Correction



a. Data Set 07 (Base Line) Mach Contours



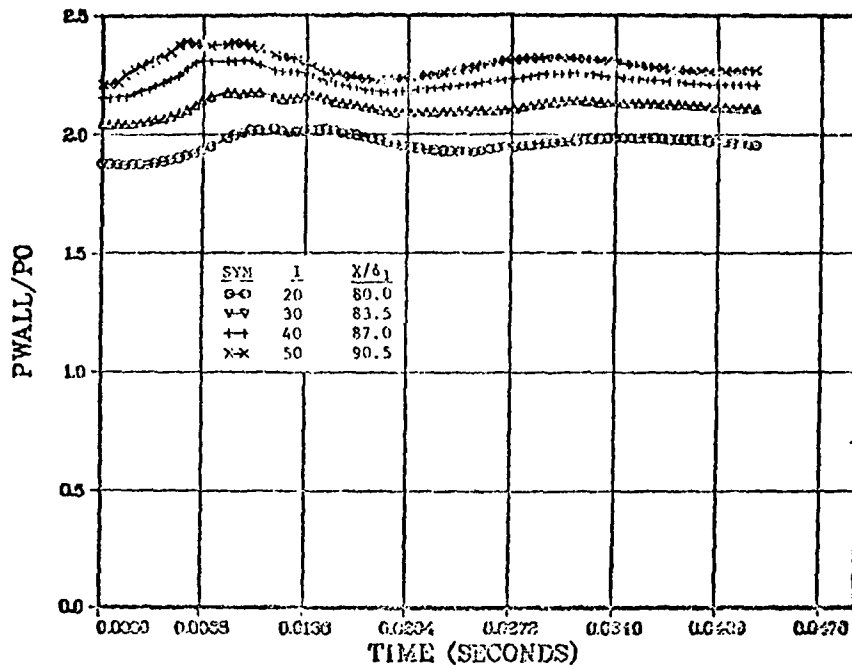
b. Data Set T200 Mach Contours

Figure 16. Mach Contours Depicting Improved Shock-Center Line Structure With Corrected Outflow Mass Rate (O & T - Series)

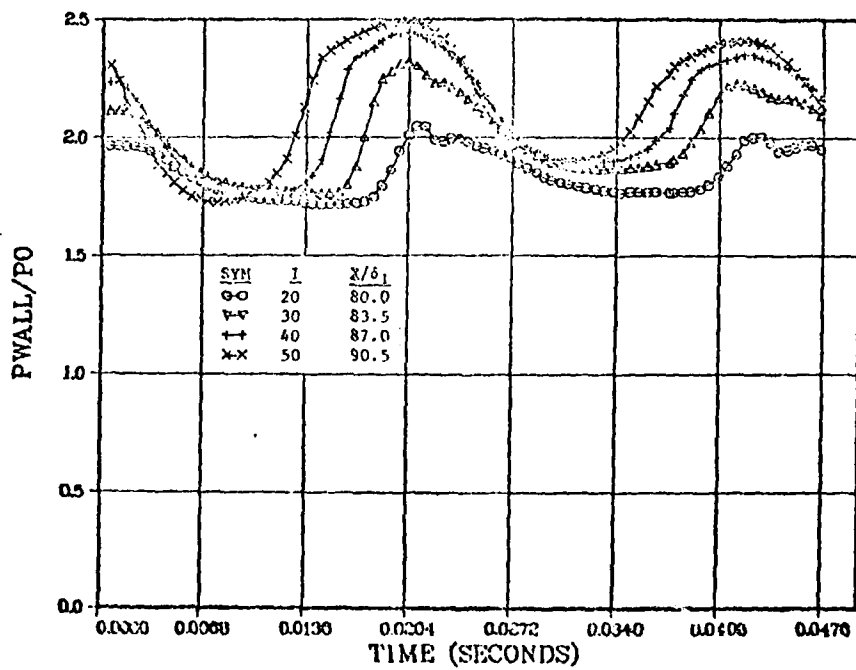
flow was higher at the outflow boundary than at the inflow boundary, the shock was distorted as if the shock wave were being pushed downstream from the fixed location on the center line boundary. Several other cases were checked and the trend of these two cases was consistently found. When the mass flow was low, the local velocity was low and the local pressure was high. Therefore, a loss of mass flow in the duct resulted in the outflow pressure being too high.

An attempt to correct the effective mass flow imbalance was made. The outflow boundary was assumed to be sufficiently far downstream that the ρu distribution can be assumed similar for the last two streamwise mesh locations. The total mass flow was computed at the inflow boundary and at the ILM1 mesh station. The ratio of these two totals was used to scale the ILM1 ρu values to compute outflow ρu values which forced a global mass flow balance at the inflow and outflow boundaries. This condition replaced the base line $(u)_x = 0$ condition at the outflow boundary in computing the T-series results. Figure 16b shows that the mass flow correction at the outflow boundary has almost totally eliminated the shock distortion at the center line boundary. Examination of the dashed line results (T-series) in Figure 14 shows small improvements in agreement with experimental results in the near shock region and an almost equal degrading of agreement for the downstream profiles. A comparison of the convergence plot for the T-series (Fig 17a) with base line plot (Fig 5, page 20) shows a three-to-fourfold increase in time required to reach a converged solution.

The last computation to be performed was an attempt to apply the outflow mass correction to the modified duct three-dimensional case. These calculations were denoted as the U-series. Figure 17b shows that the convergence of the U-series was far from complete and Figure 18 reveals that

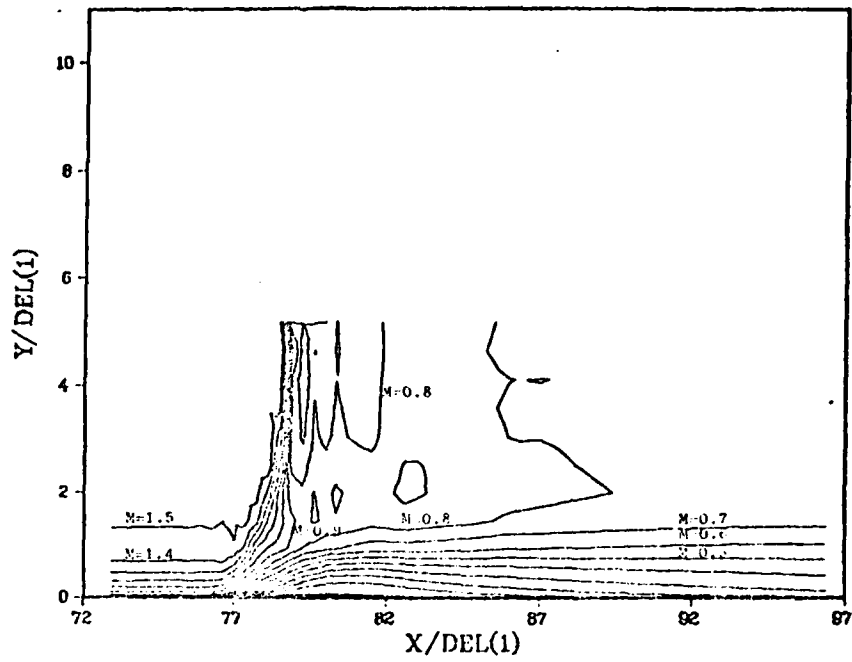


a. T - Series

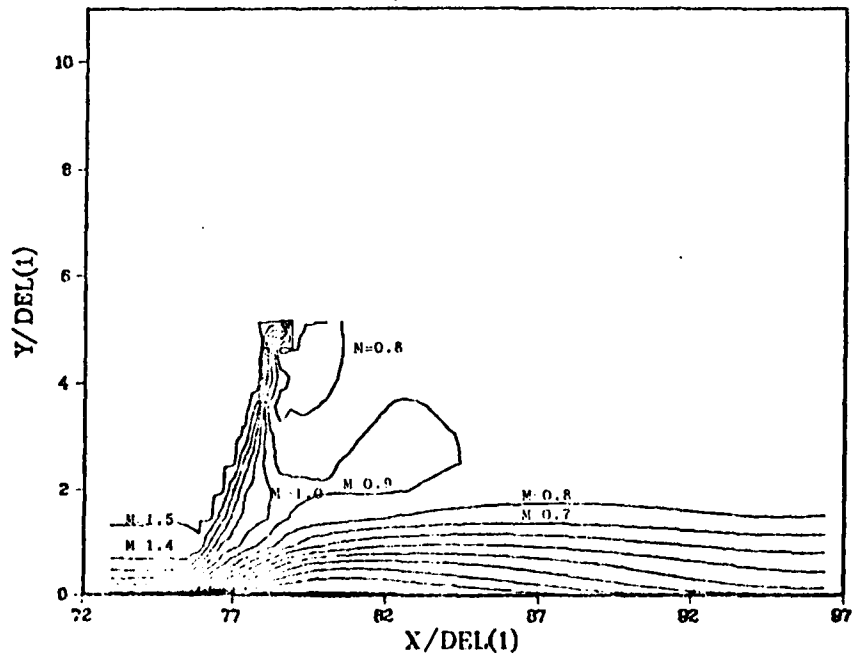


b. U - Series

Figure 17. Convergence Plots for T and U Series Computations



a. Data Set U000 Mach Contours



b. Data Set U200 Mach Contours

Figure 18. Mach Contours Depicting Shock Movement with Attempted 3-D and Mass Flow Rate Corrections (U-Series)

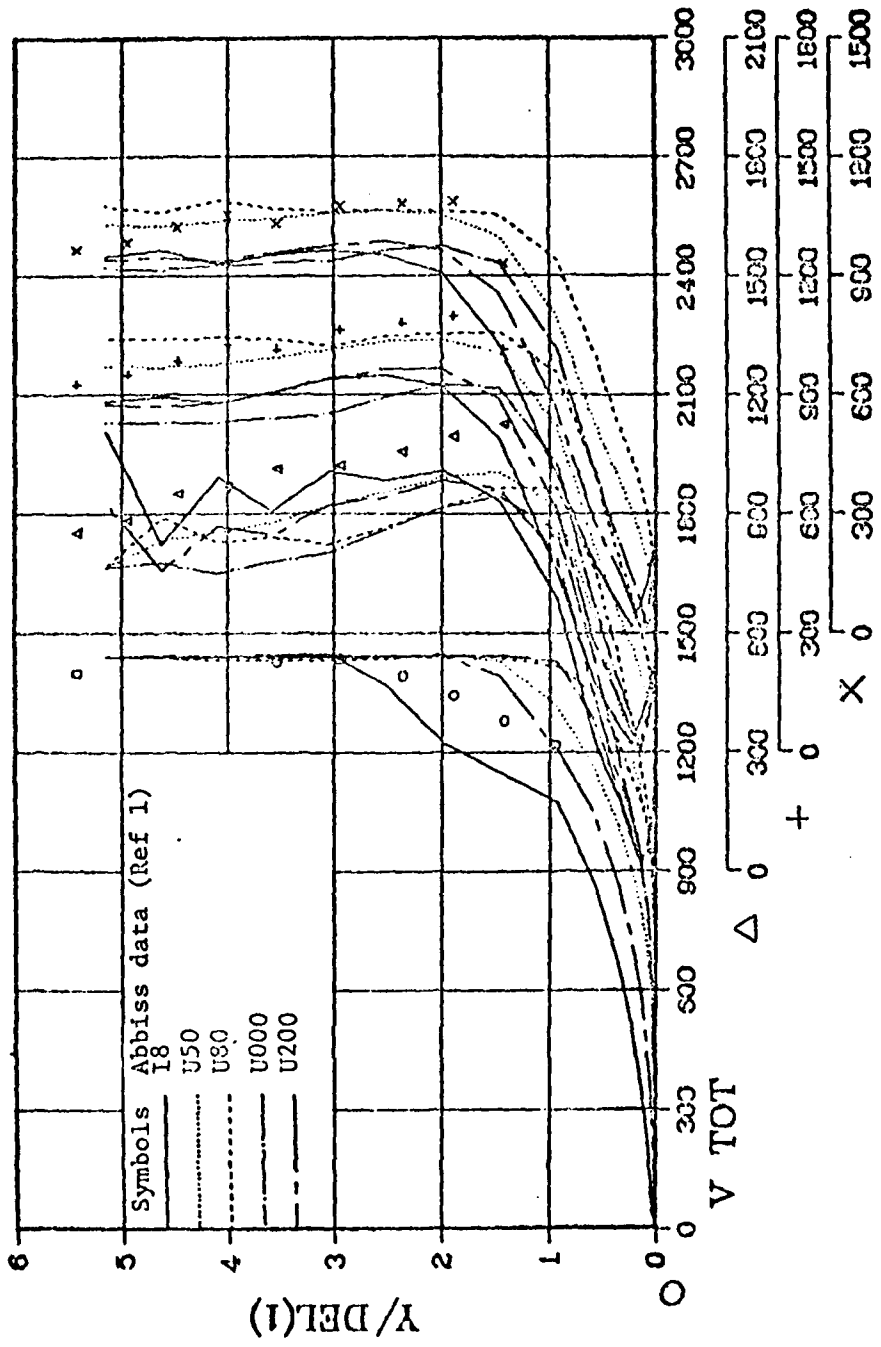


Figure 19. Transverse Total Velocity Profiles of Sequential Numerical Results Compared to Experiment (U-Series)

the shock was oscillating in the duct. However, Figure 19 indicates that the flow was oscillating around the experimental data. This gives encouragement that a three-dimensional correction of this type is feasible. The convergence of the U-series is too slow to justify continued computations without attempting to improve the convergence rate. Approximately 8 hours of computer processor time is represented on Figure 17b. A very rough damping ratio convergence prediction calculation indicated that at least another 30 hours would be required to converge the solution at the present rate.

Conclusions

The results are summarized by the following conclusions:

1. The two-dimensional MacCormack code yields results that are in qualitative and quantitative (approximately 10%) agreement with the experimental results of Abbiss. This agreement has been demonstrated for both strong and weak transonic interactions.
2. The experimental data exhibits measurable three-dimensional effects which if accounted for in the numerical model or eliminated from the experimental approach would bring the experimental and numerical results into even better agreement.
3. Strong and weak transonic normal shock turbulent boundary layer interactions can be computed without any modification to boundary condition treatment.
4. The subsonic outflow boundary treatment is very important. A mathematically consistent formulation to the outflow can be physically incompatible with the computational algorithm and not only affect the solution by actually prevent convergence.

5. The use of a two-dimensional code to provide useful engineering results for a three-dimensional duct flows is both feasible and promising.

6. A more efficient method to reduce computing time is very desirable, especially for cases where three-dimensional effects are required in the simulation.

IV. Recommendations and Suggestions

1. Further work is needed relative to boundary conditions and their numerical implementation, especially for subsonic boundaries.

2. Effort should be continued to determine a method to implement the shock wave, maintain a constant global mass flows, and insure a reasonable outflow pressure for this highly coupled problem.

3. The computation of the U-series (three-dimensional correction) should be continued with an improved convergence scheme if possible.

4. More of the experimental results should be obtained from East and Abbiss and compared to the numerical results to provide a more complete analysis base.

5. A single case should be computed with an increased number of mesh points (refined mesh structure) to provide a better check on resolution effects.

6. A two-dimensional supersonic duct computation would provide a better inflow boundary condition for the simulation than the boundary layer code used to date.

7. Application of other finite difference codes or a finite element technique, would provide another comparison with the present methods.

8. A careful analysis of existing experimental data should be conducted to determine if there is truly a post-shock supersonic zone. A new experimental effort may well be required to resolve this basic question.

Bibliography

1. Abbiss, J. B., et al. "A Study of the Interaction of a Normal Shock Wave and a Turbulent Boundary Layer Using a Laser Anemometer," RAE TR 75141, Bedford, United Kingdom, December 1975.
2. Ackeret, J. et al. "Investigation of Compression Shocks and Boundary Layers in Gases Moving at High Speed," NASA Langley Research Center, VA, TM-1113, January 1947.
3. Allen, J. S. and S. I. Cheng. "Numerical Solution of the Compressible Navier-Stokes Equations for the Laminar Near Wake," The Physics of Fluids, 13(1):37-52, (January 1970).
4. Altstatt, M. C. "An Experimental and Analytic Investigation of a Transonic Shock-Wave/Boundary-Layer Interaction," Arnold Air Force Station, Tenn., AEDC-TR-77-47, May 1977.
5. Beauregard, A. J. "An Analytical Study of the Effects of Mass Transfer on a Compressible Turbulent Boundary Layer," Thesis GA/MC/76D-3, Air Force Institute of Technology, Wright-Patterson AFB, Ohio, December 1976.
6. Coakley, T. J., et al. "Evaluations of Turbulent Models for Three Primary Types of Shock Separated Boundary Layers," AIAA Paper 77-692, June 1977.
7. East, L. F. "The Application of a Laser Anemometer to the Investigation of Shock-Wave Boundary-Layer Interaction, AGARD Conference Proceedings No. 193, 1976.
8. Gadd, G. E. "The Interactions Between Wholly Laminar or Wholly Turbulent Boundary Layers and Shock Waves Strong Enough to Cause Separation," Journal of the Aeronautical Sciences, 20: 729-747, January 1953.
9. Green, J. E., "Interactions Between Shock Waves and Turbulent Boundary Layers," RAE TR 69098, Farmborough, United Kingdom, May 1969.
10. Inger, G. R. and W. H. Mason. "Analytical Theory of Transonic Normal Shock-Turbulent Boundary-Layer Interaction," AIAA Journal, 14: 1266-70 (September 1976).
11. Inger, G. R. "Analysis of Transonic Normal Shock-Boundary Layer Interaction and Comparison with Experiment," AIAA Paper 76-331, July 1976.
12. Kooi, J. W. "Experimental on Transonic Shock Wave Boundary Layer Interactions," AGARD Conference Proceedings No. 168, 1975.
13. Liepmann, H. W. "The Interaction Between Boundary Layer and Shock Waves in Transonic Flow," Journal of Aeronautical Sciences, 13: 623-637, December 1946.
14. MacCormack, R. W. "An Efficient Numerical Method of Solving the Time-Dependent Compressible Navier-Stokes Equations at High Reynolds Number," TMX-73-129, NASA Ames Research Center, Calif., July 1976.

15. Mason, N. G. and G. R. Inger. "Analytical Study of Transonic Normal Shock-Boundary Layer Interaction," AIAA Paper 75-831, June 1975.
16. Materr, G. G. and J. R. Viegas. "A Normal Shock-Wave Boundary Layer Interaction at Transonic Speed," AIAA Paper 76-161, January 1976.
17. Melnick, R. and M. Grossman. "Analysis of the Interaction of a Weak Normal Shock Wave with a Turbulent Boundary Layer," AIAA Paper 74-598, June 1974.
18. Panas, A. G. "Calculation of a Boundary Layer Interacting with a Normal Shock by a Discontinuity Analysis," Rhode Saint Genese, Belgium: von Karman Institute for Fluid Mechanics, TN 121, October 1976.
19. Pearcey, H. H. "Shock-Induced Separation and Its Prevention by Design and Boundary Layer Control," Boundary Layer and Flow Control, Volume 2, Edited by G. V. Lackmann. New York: Pergamon Press, 1961.
20. Roach, R. L. "An Implicit Finite Difference Procedure for the Laminar, Supersonic Base Flow," Ph.D. Thesis, Georgia Institute of Technology, December 1977.
21. Roache, P. J. Computational Fluid Dynamics. Albuquerque, New Mexico: Hermoas Publishers, 1972.
22. Schlichting, H. Boundary Layer Theory. New York: McGraw Hill, Inc., 1968.
23. Schofield, W. H. "Turbulent Boundary Layers in Compressible Flow and Their Interactions with Normal Shock Waves - A Survey and Proposed Investigation," ARL Mechanical Engineering Note 21, Melbourne, Australia, October 1970.
24. Seddon, J. "The Flow Produced by Interactions of a Turbulent Boundary Layer with a Normal Shock of Strength Sufficient to Cause Separation," R & M No. 3502 (Previously published as TM Aero 667, March 1960) Bedford, United Kingdom, March 1970.
25. Shang, J. S. and W. L. Hankey Jr. "Numerical Solution of the Navier-Stokes Equations for a Three-Dimensional Corner," AIAA Journal, 15 (11): 1575-82 (November 1977).
26. ----- "Numerical Simulation of Shock Wave-Turbulent Boundary-Layer Interaction," AIAA Journal, 14(10): 1451-57 (October 1976).
27. ----- "Numerical Solution for Supersonic Turbulent Flow Over a Compression Ramp," AIAA Journal, 13(10) 1368-74 (October 1975).
28. Shea, J. R. III. "A Numerical Study of Transonic Normal Shock-Turbulent Boundary Layer Interactions," AIAA Paper 78-1170, July 1978.
29. ----- Instructor and Initial Thesis Advisor (unpublished calculations). School of Engineering, Air Force Institute of Technology, Wright-Patterson AFB, 1979.

30. Viegas, J. R. and T. J. Coakley. "Numerical Investigation of Turbulent Models for Shock Separated Boundary-Layer Flows," AIAA Journal, 16(4): 283-294.
31. Viegas, J. R. and C. C. Horstman. "Comparison of Multiequation Turbulence Models for Several Shock Separated Boundary-Layer Interaction Flows," AIAA Paper 78-1165, July 1978.
32. Winter, K. G. Letter from Fluid Mechanics Division, Royal Aircraft Establishment, Bedford, United Kingdom to J. Shea, AFIT, (RAE Ref BTA 38/104) 31 May 1979.

Appendix A

A Description Of The Finite Difference Method Used

The finite difference code used for this study was based on the method of MacCormack (Ref 14). The code is a hybrid implicit-explicit scheme to solve the Navier-Stokes equations in two dimensions. The program is similar to that employed by Shea (Ref 28), but incorporates different boundary conditions. The procedure will be discussed in terms of grid generation, numerical algorithms, and turbulence model. Boundary conditions are discussed separately in Sections II and III with supporting equation development in Appendix B.

The computational domain was divided into a 64 x 32 rectangular mesh system. The streamwise x-direction was divided into an equally spaced Δx mesh by 64 grid points. The spacing was such that the ratio of Δx to inflow boundary layer thickness is approximately 0.37. Any deviation from this spacing was specifically noted. The normal shock wave was introduced into the flow field between the streamwise grid points 16 and 17 where the Rankine-Hugonist conditions was applied. A description of the shock implementation was given in Section III.

The y-direction was divided into two regions. Points adjacent to the wall were exponentially spaced up to approximately 1.2 times the inflow boundary layer thickness. In the outer region, the points were equally spaced. Most of the calculations were accomplished with 32 grid points in the y-direction of which 14 were in the fine mesh region. The exponential spacing was generated by

$$\Delta y = \frac{e^{ck\eta} - 1}{e^{ck} - 1}$$

A-1

where
$$\eta = \frac{(J - 1.5)}{(JLPM - 1)}$$

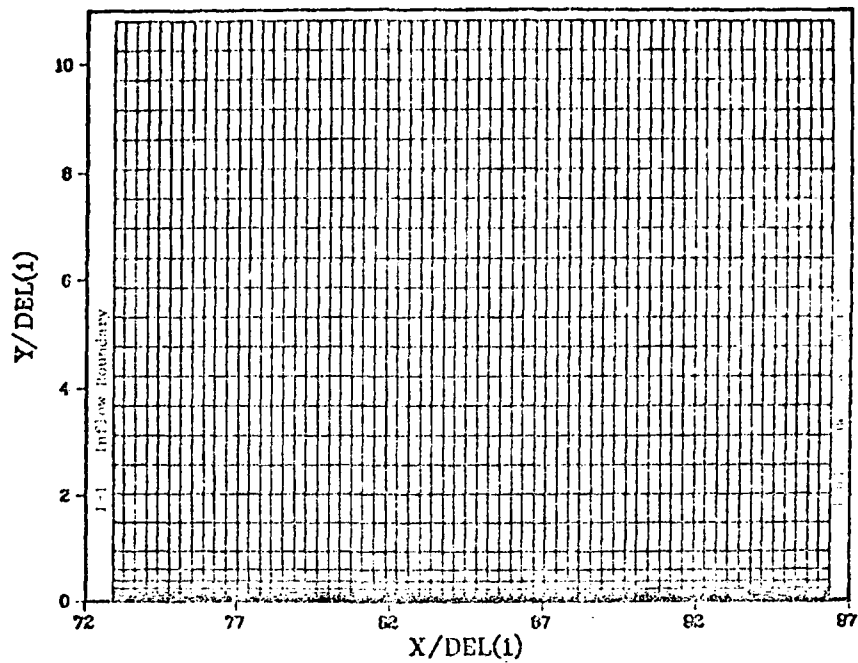
So, ck was a constant and η is a nondimensional value of y to position the $J = 1$ and $J = 2$ grid points at $\pm 0.5 \Delta y$ for the reflexion plane implementation of the wall boundary conditions. $JLPM$ was the last grid point in the fine mesh. This relationship provided a mesh in which each Δy was approximately 0.6, the height of the Δy above it. The value of ck was adjusted to provide a smooth transition between the fine mesh height and the constant mesh size in the outer region. The criteria used was that Δy in the interface mesh (between $J = 14$ and $J = 15$) was approximately the average of the spacing just above and below. This resulted in the interface size of approximately $0.8 \Delta y$ of the outer region. See Figure 20 for the resulting mesh structure.

The exponentially spaced mesh adjacent to the wall allowed better computational resolution in the viscous dominated region where high gradients occur along with separation and reattachment when present. Further, the fine mesh was spaced so that the first two points at the wall were kept in the linear viscous subregion of the boundary layer. Appendix B describes the wall boundary implementation. The small y increments close to the wall require consideration in computational algorithm development.

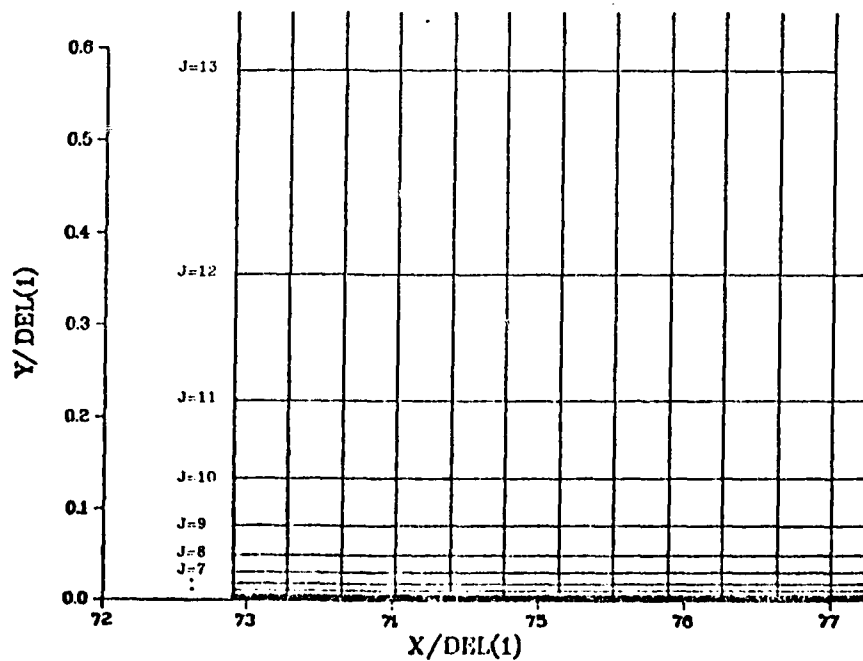
The two-dimensional time-dependent compressible Navier-Stokes equations, A-2, were expressed in the flux vector form.

$$(U)_t + (F)_x + (G)_y = 0 \quad \text{A-2}$$

where



a. Total Computational Domain



b. Detailed Mesh Structure Near the Wall

Figure 20. Computational Mesh Structure

$$U = \begin{pmatrix} \rho \\ \rho u \\ \rho v \\ e_t \end{pmatrix}, \quad F = \begin{pmatrix} \rho u \\ \rho u^2 + \sigma_x \\ \rho uv + \tau_{xy} \\ (e_t + \sigma_x)u + \tau_{yx}v - k(e_i)_x \end{pmatrix}$$

$$G = \begin{pmatrix} \rho v \\ \rho uv + \sigma_{yx} \\ \rho v^2 + \tau_y \\ (e_t + \sigma_y)v + \tau_{xy}u - k(e_i)_y \end{pmatrix}$$

$$\sigma_x = p - \lambda[(u)_x + (v)_y] - z\mu (u)_x$$

$$\sigma_y = p - \lambda[(u)_x + (v)_y] - z\mu (v)_y$$

and

$$\tau_{xy} = \tau_{yx} = -\mu[(u)_y + (v)_x]$$

The algorithm used to solve A-2 is quite different for the coarse and fine mesh regions. The fine mesh method was more complex but provided significantly improved computing efficiency for the extremely small y increments close to the wall. For the coarse mesh the dependent variables ρ , ρu , ρv , and e_t were estimated at a given time $t = n\Delta t$ at each grid point i, j . The solution was then computed at time $t = (n+1)\Delta t$ by

$$U_{i,j}^{n+1} = L(\Delta t) U_{i,j}^n \quad \text{A-3}$$

where L was a sequence of operators which explicitly advanced the solution Δt in time. A-3 was repeated until the change in U between time n and $n+1$ was small enough to assume the solution is satisfactorily converged (See Section III for convergence criteria) to a steady state solution. The advance was time-split into two primary operators.

L_x advances

$$(U)_t + (F)_x = 0 \quad A-4$$

and L_y advances

$$(U)_y + (G)_y = 0 \quad A-5$$

The one dimensional difference operators L_x and L_y were cast into a symmetric sequence

$$U_{i,j}^{n+1} = L_x\left(\frac{\Delta t}{2}\right) L_y(\Delta t) L_x\left(\frac{\Delta t}{2}\right) U_{i,j}^n \quad A-6$$

Thus, the L_x operator was called twice to advance the solution one half Δt each time according to A-4 with U and F as defined in A-1. Between the two L_x steps of A-4 L_y was advanced Δt according to A-5. The combined effect of these three sequential split operations contributed to the advance of A-1 for a time Δt (Ref 7).

The time Δt was determined according to the numerical stability analysis criteria of the explicit operators. The Δt for each step was proportional to the x and y mesh spacing. In the exponentially spaced region, the spacing in Δy become very small and the allowable Δt was proportionally small. Therefore, to improve efficiency a more complex algorithm was used in this region.

The fine mesh algorithm further subdivided L_y into its L_{y_H} inviscid (hyperbolic) terms and L_{y_p} viscous (parabolic) terms.

L_{y_H} advances

$$(U)_y + (G_H)_y = 0 \quad A-7$$

where

$$G_H = \begin{pmatrix} \rho v \\ \rho u v \\ \rho v v + p \\ (e_t + p)v \end{pmatrix}$$

by an explicit approach using characteristic relations to predict convection and pressure fields and was stable provided

$$\Delta t \leq \frac{\Delta y}{|v|}$$

This resulted in a much larger allowable time step because as Δy becomes very small close to the wall v is also approaching zero. The result was stable time steps which were 50 to 100 times larger than otherwise possible (Ref 14:7).

L_{y_p} advances

$$(U)_t + (G_p)_y = 0 \quad \text{A-8}$$

where

$$G_p = G - G_H$$

by an implicit procedure of either Crank-Nicolson or Laasonen type. The second-order accurate Crank-Nicolson method was used when $\mu\Delta t/dy^2$ was small enough to preclude erratic behavior. When this quantity was large enough to cause numerical instability, the first order Laasonen method was used.

The L_{y_p} and L_{y_H} operators were incorporated in the fine mesh as

$$U_{i,j}^{n+1} = [L_{y_H}(\frac{\Delta t}{2m}) L_{y_p}(\frac{\Delta t}{2m}) L_x(\frac{\Delta t}{m}) L_{y_p}(\frac{\Delta t}{2m}) L_{y_H}(\frac{\Delta t}{2m})]^m U_{i,j}^n$$

where m was the number of fine mesh time step required to equal one course mesh time step. Thus, the fine mesh was advanced by five sequential operators m times every time the coarse mesh was advanced by time Δt .

All of the operators were conservative and Δt was computed for each step to insure numerical stability. Ref 14 provided a much more complete description of the numerical operators used for this effort.

The turbulence model used was the algebraic eddy viscosity model used by Shea (Ref 28). It was a modified Cebeci-Smith-Mosinakis model in the inner layer and a Maise-McDonald model in the law of the wake region. References 6, 30, and 31 indicated that this model was probably most appropriate and the incorporation of more complex schemes would not result in improved solutions.

Appendix B

Boundary Condition Supporting Equations

Wall Boundary Finite Difference Equations

The reflection plane implementation at the wall of,

$$v = u = (T)_y = 0 \quad \text{B-1}$$

with $J = 1$ at $-0.5 \Delta y(1)$ and $J = 2$ at $+0.5 \Delta y(1)$ from the wall was:

$$u(I, 1) = -u(I, 2) \quad \text{B-2}$$

$$v(I, 1) = -v(I, 2) \quad \text{B-3}$$

$$EI(I, 1) = EI(I, 2) \quad \text{B-4}$$

where EI denotes specific internal energy.

The compatible condition for the normal (y) momentum equation at the wall Eqn II-3 was implemented (after Ref 26) to provide pressure at the wall by:

$$\begin{aligned}
 P_{i, 1} &= P_{i, 2} \\
 &- \frac{\Delta y [\mu_{i+1} (u_{i+1,3} - u_{i+1,1}) - \mu_{i-1} (u_{i-1,3} - u_{i-1,1})]}{2\Delta x (y_3 - y_1)} \\
 &+ \frac{\lambda_i [(u_{i+1,2} - u_{i-1,2}) - (u_{i+1,1} - u_{i-1,1})]}{2\Delta x \Delta y} \\
 &+ (\lambda_i + 2\mu_i) \frac{\frac{(v_{i,3} - v_{i,2})}{y_3 - y_2} - \frac{(v_{i,2} - v_{i,1})}{\Delta y}}{0.5(y_3 - y_1)}
 \end{aligned} \quad \text{B-5}$$

Center Line Boundary

The steady 2-D governing equations assuming the flow to be inviscid and adiabatic at the center line were:

Continuity

$$(\rho u)_x + (\rho v)_y = 0 \quad \text{B-6}$$

x-momentum

$$(\rho u^2)_x + (\rho uv)_y + (p)_x = 0 \quad \text{B-7}$$

y-momentum

$$(\rho uv)_x + (\rho v^2)_y + (p)_y = 0 \quad \text{B-8}$$

energy

$$(\rho u e_t)_x + (\rho v e_t)_y = 0 \quad \text{B-9}$$

Applying continuity (B-6) to B-7, 8, and 9 yields:

$$\rho u(u)_x + \rho v(u)_y + (p)_x = 0 \quad \text{B-10}$$

$$\rho u(v)_x + \rho v(v)_y + (p)_y = 0 \quad \text{B-11}$$

$$\rho u(e_t)_x + \rho v(e_t)_y = 0 \quad \text{B-12}$$

Introducing the $v=0$ condition at the center into B-6, 10, 11 and 12 yield:

$$(\rho u)_x + (v)_y = 0 \quad \text{B-13}$$

$$\rho u(u)_x + (p)_x = 0 \quad \text{B-14}$$

$$(p)_y = 0 \quad \text{B-15}$$

$$(e_t)_x = 0 \quad \text{B-16}$$

Therefore, $(e_t)_x = 0$ can be added to the list of compatible center line boundary conditions.

YITA

Lowell C. Keel was born on 2 April 1942 in Harrisburg, Illinois. He was graduated from high school in June 1960 in Carrier Mills, Illinois. Upon graduation in December 1965 from Southern Illinois University at Carbondale, he received a reserve USAF commission via the ROTC program. Reporting to active duty in October 1966, he served over four years in the External Aerodynamics Group, Flight Mechanics Division, of the Air Force Flight Dynamics Laboratory. In 1970, he was selected as a Laboratory Associate assigned to the NASA Ames Research Center, Moffett Field, California where he served as a NASA wind tunnel test conductor and project engineer for over two years. Subsequently, he was assigned to the 1137 Special Activity Squadron HQ USAF and detailed to NASA Dryden Flight Research Center, Edward AFB, California. At Dryden his primary duty was as the NASA Project Engineer and Technical Director for the joint NASA/USAF Transonic Aircraft Technology (TACT) Program. In August 1976, he was assigned to the A-10 System Program Office (SPO) in the Aeronautical Systems Division, W-PAFB, Ohio where he served as a Configuration Manager until his entry into the School of Engineering, Air Force Institute of Technology, in June 1978.

Permanent address: 215 S. McKinley Street
Harrisburg, Illinois 62946

UNCLASSIFIED

SECURITY CLASSIFICATION OF THIS PAGE(When Data Entered)

boundary, but a simple zero gradient condition gave satisfactory results at four different outflow boundary positions relative to the shock wave. Numerical results ($M = 1.51, 1.40$ and 1.30 $Re = 3 \times 10^6$ per ft) were compared with the experimental data reported by Abbiss and East. Even though the data exhibit three-dimensional effects, the two-dimensional computations show agreement within approximately 10%. The difference observed in the numerical-experimental comparisons were all consistent with expected three-dimensional trends. Although not conclusive, the potential of adding simple three-dimensional corrections to the two-dimensional code shows promise for improving the experimental-numerical agreement.

UNCLASSIFIED